Title

Degraded tactile coding in the Cntnap2 mouse model of autism.

Permalink

Journal

Authors

Wang, Han

Feldman, Daniel

Publication Date

DOI

Degraded tactile coding in the Cntnap2 mouse model of autism

Han Chin Wang[1], **Daniel E. Feldman**[1,2,*]

[1]Department of Molecular & Cell Biology and Helen Wills Neuroscience Institute, University of California, Berkeley, Berkeley, CA 94720, USA

[2]Lead contact

SUMMARY

Atypical sensory processing is common in autism, but how neural coding is disrupted in sensory cortex is unclear. We evaluate whisker touch coding in L2/3 of somatosensory cortex (S1) in *Cntnap2*^{−/−} mice, which have reduced inhibition. This classically predicts excess pyramidal cell spiking, but this remains controversial, and other deficits may dominate. We find that c-fos expression is elevated in S1 of *Cntnap2*^{−/−} mice under spontaneous activity conditions but is comparable to that of control mice after whisker stimulation, suggesting normal sensory-evoked spike rates. GCaMP8m imaging from L2/3 pyramidal cells shows no excess whisker responsiveness, but it does show multiple signs of degraded somatotopic coding. This includes broadened whisker-tuning curves, a blurred whisker map, and blunted whisker point representations. These disruptions are greater in noisy than in sparse sensory conditions. Tuning instability across days is also substantially elevated in *Cntnap2*^{−/−}. Thus, *Cntnap2*^{−/−} mice show no excess sensory-evoked activity, but a degraded and unstable tactile code in S1.

Graphical abstract
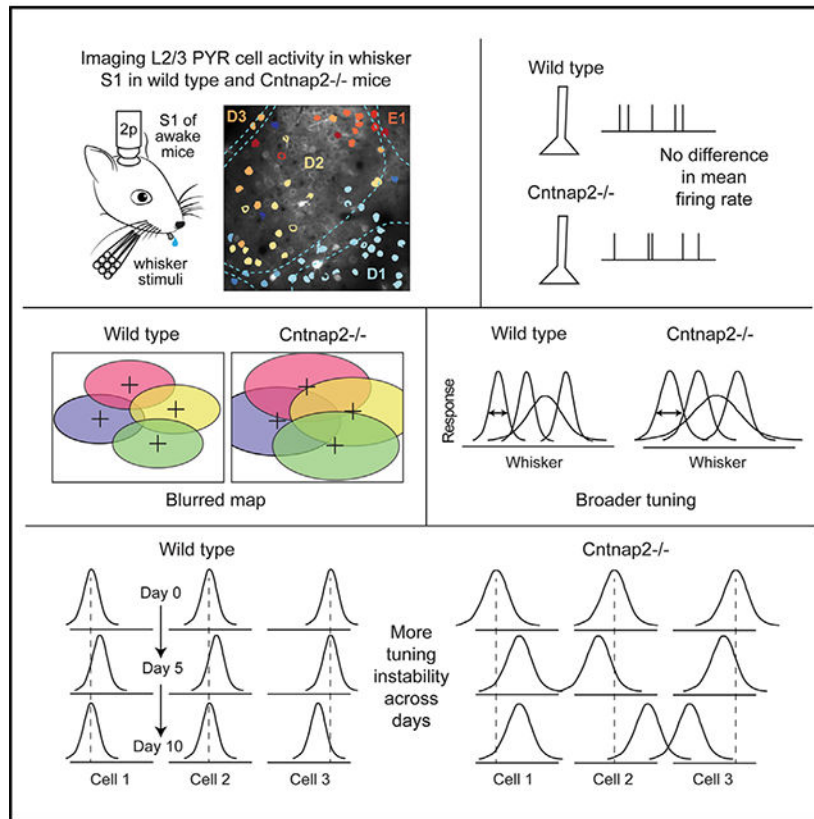
In brief

Wang and Feldman characterize tactile coding abnormalities in whisker S1 cortex in the *Cntnap2*^{−/−} mouse model of autism. These mice show multiple signs of degraded sensory coding, including blurred maps and unstable tuning, but not excess spiking. Impaired discriminative coding may be a common feature of the sensory cortex in autism.

INTRODUCTION

How neural circuit dysfunction leads to the sensory and cognitive phenotypes of autism spectrum disorder (ASD) remains elusive. Because many ASD risk gene mutations reduce parvalbumin (PV) interneuron function and increase the excitation:inhibition (E:I) ratio in the cerebral cortex, a dominant circuit-level model has been that cortical circuits exhibit hyperexcitability and excess pyramidal (PYR) cell spiking in ASD. Such excess spikes could increase noise in neural coding, thus impairing information processing.[1,2] Alternatively, PV hypofunction or other ASD-related circuit changes could drive other forms of neural coding impairment without any excess PYR spiking—for example, broadening neural tuning, degrading cortical maps, disrupting cortical rhythms or precise spike timing, or degrading the structure of population codes. Distinguishing degraded coding from hyperexcitability models of circuit dysfunction in ASD has important implications for the development of therapeutic strategies.

The sensory cortex is a useful site to investigate circuit dysfunction in autism, because atypical sensory processing occurs in up to 90% of individuals with ASD.[3] Across different transgenic mouse models of ASD, PV hypofunction is common in the sensory cortex in many models, but excess PYR spiking is rare, and instead various forms of degraded neural coding have been observed.[4] Excess spiking occurs in *Shank3b*^{−/−} mice, and in some sensory cortical areas in *Fmr1*[−/y] mice.[5–8] However, spike rates are normal or reduced in the sensory cortex of many other ASD models, including *MeCP2*^{−/−}, *Syngap1*^{+/−}, and *16p11.2* deletion, and in other primary sensory areas in *Fmr1*[−/y], raising the question of what may underlie abnormal sensory detection or discrimination behavior in these models.[9–13] The goal of the current study is to characterize neural coding phenotypes in the primary somatosensory cortex (S1) in the *Cntnap2*^{−/−} mouse model of autism. We focused on S1 because tactile abnormalities are common in autism and may contribute to development of social deficits,[14–16] and CNTNAP2 is expressed in mouse brain areas engaged in sensory processing.[17]

The *CNTNAP2* gene encodes Contactin-associated protein 2 (CASPR2), a cell adhesion molecule that localizes at the axon initial segment and nodes of Ranvier, and clusters K_v1 channels to regulate spiking excitability.[18] *CNTNAP2* is an autism risk gene. Loss-of-function mutations of *CNTNAP2* cause Pitt-Hopkins-like syndrome 1 (OMIM: 610042), which includes autistic symptoms, and SNPs in *CNTNAP2* genes are associated with the increased susceptibility of autism.[19–21] *Cntnap2*^{−/−} mice[22,23] show social, communication, and repetitive motion behavioral phenotypes,[23,24] as well as atypical tactile, auditory, olfactory, and visual processing.[17,25–30]

Cntnap2^{−/−} mice show weakened synaptic inhibition and excitation in S1 and other cortical areas[13,31–35] and strong evidence for PV hypofunction. In layer (L) 2/3 of S1, whisker-evoked spiking of PV cells and PV-mediated feedforward inhibition are reduced.[13,30,31,36,37] However, whether *Cntnap2*^{−/−} mice exhibit excess spiking in sensory cortex is unclear. Prior studies of single-unit spiking reported normal spiking in S1[13] and weaker-than-normal spiking in visual cortex (V1),[28] but excess spiking has been suggested from c-fos staining and multi-unit spike recording in S1 and auditory cortex (A1).[29,38] We sought to resolve whether S1 exhibits excess spiking in *Cntnap2*^{−/−} mice, and if not, to test for other types of neural coding abnormalities that may occur.

Detection of coding abnormalities is aided in whisker S1 by the detailed understanding of whisker tuning and whisker map organization in wild-type mice. S1 neurons have narrow somatotopic tuning for one or a few neighboring whiskers on the face. L4 barrels mark anatomical columns, one for each whisker in a precise anatomical somatotopic map.[39] Within L4, nearly all neurons are tuned for their columnar whisker (CW). In L2/3, PYR neurons tuned to different whiskers are intermixed in each column, but the most common tuning is for the CW, resulting in an L2/3 whisker map with correct average topography, but high local scatter.[40–42] As a result, the set of neurons tuned for a given whisker is distributed across several columns, centered on the whisker's anatomical column. Interestingly, the somatotopic tuning of many L2/3 PYR neurons is markedly unstable over days and weeks, an example of representational drift.[42] Such tuning drift is found in several primary sensory

cortical areas as well as multiple high-order association cortices, and thus is an important feature of cortical population codes.[43–45]

We characterized sensory coding in S1 of *Cntnap2*^{−/−} and wild-type (*Cntnap2*^{+/+}) mice, using two-photon calcium imaging in awake mice receiving calibrated whisker sensory stimuli. We also used c-fos immunostaining to assess gross changes in neural activity in S1. The results showed that *Cntnap2*^{−/−} mice do not exhibit excess sensory-evoked activity in L2/3 PYR cells in S1. Instead, they show several forms of degraded sensory coding, including broadened single-neuron tuning, substantially degraded map topography, and elevated tuning instability.

RESULTS

Whisker-evoked activity in L2/3 of S1 measured by c-fos expression

We assayed for gross alterations in S1 cortical activity in *Cntnap2*^{−/−} mice by the expression of the immediate-early gene *c-fos*[46,47] in L2/3. Mice were lightly anesthetized and head-fixed, and whiskers on the right side of the face in the A, C, and E rows, plus associated beta and delta whiskers, were inserted into a piezoelectric actuator array. Calibrated deflections were applied to these whiskers for 30 min (0.5-s deflection trains, delivered every 5 s). After 60–90 min recovery, mice were euthanized, and flattened sections were made from S1, parallel to L4, from both the contralateral hemisphere (whisker stimulated) and the ipsilateral hemisphere (treated as an unstimulated control). Sections were processed for c-fos immunofluorescence and co-stained with streptavidin to reveal L4 barrels.[48] c-fos^{+} cells were identified in L2/3, and their positions were marked relative to barrel column boundaries, identified from the L4 barrels (Figures 1A–1C). We quantified c-fos cell density in identified whisker columns, excluding cells overlying septa. In the contralateral (stimulated) hemisphere, the density of c-fos^{+} cells was higher in L2/3 of cortical columns corresponding to deflected A-C- E row whiskers, relative to columns for undeflected B-D row whiskers, in both wild-type (*Cntnap2*^{+/+}, called control) and *Cntnap2*^{−/−} mice (Figures 1B–1D) (control mice: $p < 0.001$, unbalanced two-way ANOVA, $n = 9$ columns in 3 mice; *Cntnap2*^{−/−}: $p < 0.001$, unbalanced two-way ANOVA, $n = 9$ columns in 3 mice). In the ipsilateral (unstimulated) hemisphere, c-fos cell density was equal in A-C-E vs. B-D whisker columns (Figure 1D) (control mice: $p = 0.383$; *Cntnap2*^{−/−}: $p = 0.522$). Thus, 30 min of whisker stimulation effectively activates L2/3 neurons, as assayed by c-fos expression.

In the ipsilateral, unstimulated hemisphere, *Cntnap2*^{−/−} mice showed increased density of c-fos^{+} cells in both A-C-E and B-D whisker rows relative to control mice, suggesting higher spontaneous activity (Figure 1D, ipsilateral; p values shown in the figure). In the contralateral, stimulated hemisphere, whisker stimulation evoked similar c-fos density in A-C-E columns of control and *Cntnap2*^{−/−} mice, with only a modest, non-significant trend for increased density in *Cntnap2*^{−/−} mice (Figure 1D, left). Whisker stimulation also modestly increased c-fos cell density in B-D rows of the stimulated hemisphere (Figure 1D, right), consistent with salt-and-pepper somatotopy in L2/3.[40–42,49] *Cntnap2*^{−/−} mice showed a greater density of c-fos cells in B-D rows of the stimulated hemisphere than control mice, suggesting that the whisker map might become more spatially distributed or blurred in L2/3 of *Cntnap2*^{−/−} mice (Figure 1D, right).

We normalized c-fos cell density in each contralateral hemisphere to the ipsilateral, unstimulated hemisphere of the same mouse to infer signal-to-noise ratio for whisker-evoked neural activation over spontaneous activity. Control and *Cntnap2*^{−/−} mice showed indistinguishable multiplicative increases in c-fos cell density after whisker stimulation (Figure 1E), both for A-C-E and B-D columns, suggesting that the signal-to-noise ratio for sensory activation was not altered in *Cntnap2*^{−/−} mice, even though the number of spontaneously active cells was greater. Together, these c-fos results suggest increased spontaneous activity and a more dispersed whisker map in S1 of *Cntnap2*^{−/−} mice, but no significant increase in the magnitude of whisker-evoked sensory activation.

Two-photon calcium imaging in S1 of awake mice

To characterize sensory coding more accurately in *Cntnap2*^{−/−} mice, we performed 2-photon population Ca^{2+} imaging of whisker-evoked activity in L2/3 of S1 in awake, whisker-attentive mice. We trained 14 mice on a behavioral task that allows quantitative assessment of whisker-evoked neural responses, receptive fields, and maps by two-photon imaging during task performance.[42] Head-fixed mice had nine whiskers inserted in a 3×3 piezoelectric actuator array. Each piezo stimulated one whisker with a brief train of whisker deflections (termed a whisker cue, five impulses at 100 ms inter-impulse interval; Figure 2B). On each trial, one of 11 stimuli was presented: either one of the nine single-whisker cue stimuli, a blank (no stimulus), or an all-whisker stimulus (Figure 2A). Mice learned to lick to the all-whisker stimulus, which was rewarded (S+), but not to single-whisker cues or blanks, which were not rewarded (S−). Once mice are trained, this task design allows single-whisker cue stimuli (S−) to be used to image whisker responses and receptive fields in S1 without lick contamination or the need for a delay period.[42]

Importantly, this task was designed only to provide a consistent, whisker-attentive behavioral state in which to assay neural coding of whisker stimuli. It does not test for altered behavioral detection or discrimination of single-whisker cue stimuli that might parallel altered neural coding of single-whisker stimuli. We know mice are whisker attentive because they discriminate all-whisker from single-whisker stimuli, and they lick to all-whisker S+ stimuli prior to reward delivery (Figures 2E and S1A), which drives the bulk of behavioral performance on the task (Figures 2D and S1C). Task performance involves whisker sensation because whisker trimming abolished discrimination in control and *Cntnap2*^{−/−} mice (Figure S1B). Mice performed well when evaluated from all licks (Figure 2D) or only from licks occurring after whisker stimulus onset but before reward delivery (Figure S1C).

We hypothesized that excess spiking or degraded sensory coding may emerge in noisy sensory conditions, compared to sparse, quieter sensory conditions. To test this, we interleaved two types of behavioral sessions (Figure 2B). In sparse stimulus sessions, each trial contained only one whisker cue, amounting to one cue stimulus every 6.5 ± 1 s. In noisy stimulus sessions, small single-whisker deflections (30% of whisker cue amplitude) were applied on random, interleaved whiskers every 200 ± 100 ms throughout the trial, starting 1.5 s before whisker cue delivery. The period of noise stimulation prior to whisker cue delivery was called the prestimulus noise period. The goal of this design was to raise sensory background noise, thus complicating encoding of cue stimuli. Mice were trained in

the sparse condition only, after which sparse and noise sessions were inter-leaved (only one condition was tested per day).

Mice reached expert performance in the sparse condition, defined as hit rate >70% and false alarm rate <25%, in 10.1 ± 0.4 days after introduction of all S− stimuli ($n = 14$ mice). There was no difference in this training duration between genotypes (control: 10.1 ± 0.3 days; *Cntnap2*$^{-/-}$: 10 ± 0.7 days, $n = 7$ mice each) (Figure 2C). There was also no difference in overall task performance, measured by d-prime or reaction time for detection of all-whisker S+ stimuli, between expert control and *Cntnap2*$^{-/-}$ mice (Figures 2D, 2E, and S1C). We interpret this to indicate that both genotypes were in a similar whisker-attentive, task-engaged state during behavior.

L2/3 PYR neurons show more spontaneous activity and slightly broader tuning, but no evidence of sensory-evoked hypersensitivity

We measured sensory responses in L2/3 PYR cells by virally expressing GCaMP8m[50] and imaging in L2/3 during the task. Whisker-evoked responses and receptive fields were measured from whisker cue stimuli on the single-whisker S− trials. Trials with licks (i.e., false alarm trials) were excluded from analysis to avoid lick-related neural activity and motion artifacts. Imaged neurons were localized post hoc relative to anatomical column boundaries by reconstructing each imaging field relative to barrels in L4.[42,51] Whisker stimuli evoked strong F/F responses from L2/3 PYR cells, allowing us to assess whisker-evoked response magnitude and whisker tuning of each cell (Figures 3A and 3B).

We analyzed 5,162 PYR cells from control mice (3,579 in sparse sessions, $n = 7$ mice and 1,583 from noise sessions, $n = 4$ mice) and 4,977 cells from *Cntnap2*$^{-/-}$ animals (3,162 in sparse sessions, $n = 7$ mice and 1,815 in noise sessions, $n = 4$ mice). Average F/F in the prestimulus noise period was higher in noise sessions than in sparse sessions, suggesting that noise stimuli were effective in driving S1 activity (Figure S2A). To assess spontaneous activity, we calculated the SD of F/F for each cell within blank trials in the sparse condition, when no stimuli are present. *Cntnap2*$^{-/-}$ mice showed modestly but significantly higher values of this metric than control mice, indicating higher spontaneous activity (Figure 3C), consistent with the c-fos results. Next, we examined responses to single-whisker cue stimuli. Overall, ~30%–40% of PYR neurons were significantly whisker responsive, as expected from known sparse coding in S1.[42,52,53] The fraction of responsive cells was not significantly different between control and *Cntnap2*$^{-/-}$, or between sparse and noise conditions (control sparse: 38.5%; control noisy: 41.6%; *Cntnap2*$^{-/-}$ sparse: 33.9%; *Cntnap2*$^{-/-}$ noisy: 34.5%) (Figure 3D).

Whisker somatotopic receptive fields were generally narrow, such that for each cell, only one to three whiskers drove F/F responses that were significantly greater than on blank trials (e.g., Figures 3A and 3B). Most cells had a single best whisker (BW) that elicited a statistically stronger response than any other whisker (control sparse: 55.1% of cells; control noisy: 53.0%; *Cntnap2*$^{-/-}$ sparse: 58.5%; *Cntnap2*$^{-/-}$ noisy: 55.3%; no differences between genotype or noise condition). The remaining cells had several (usually two to three) statistically co-equal BWs. Mean rank-ordered whisker-tuning curves revealed that *Cntnap2*$^{-/-}$ mice had a slightly blunted tuning peak but normal flanks (Figure 3E), causing

a modest broadening of whisker-tuning around the BW (assessed by BW preference metric; Figure 3F). This was observed in both sparse and noisy conditions (Figures 3E and 3F).

To test for hyperexcitability of sensory-evoked responses, we identified the BW for each cell and compared the magnitude of BW-evoked F/F (Z scored to baseline activity and averaged across trials) for each whisker-responsive neuron. In sparse conditions, BW-evoked response magnitude was no different between control and $Cntnap2^{-/-}$ mice. Noisy conditions reduced the average BW-evoked response magnitude, and $Cntnap2^{-/-}$ mice showed even smaller BW-evoked F/F than control mice in noisy conditions (Figure 3G). The same was true for absolute F/F that was not Z scored to baseline (Figure S2B). In sparse conditions, neurons in both control and $Cntnap2^{-/-}$ mice responded to BW deflection on a similar fraction of trials, but in noisy conditions, $Cntnap2^{-/-}$ neurons responded on fewer trials than control mice (Figure 3H). Thus, there was no evidence for excess whisker-evoked activity in L2/3 PYR cells in S1. Instead, we found evidence for increased spontaneous activity (Figure 3C), which is consistent with the c-fos results, but normal or slightly suppressed whisker-evoked activity, and slightly broader whisker tuning curves.

Blurred whisker map in *Cntnap2^{−/−}* mice

In mice, L2/3 PYR cells tuned to different, nearby whiskers are spatially intermixed in each column, creating local tuning heterogeneity within the whisker map. To test whether whisker map topography is altered in $Cntnap2^{-/-}$, we first analyzed this tuning heterogeneity among whisker-responsive PYR cells in one column (Figure 4A). In sparse conditions, 57% of PYR neurons in each column were tuned to the CW in control mice, but only 49% were CW-tuned in $Cntnap2^{-/-}$ mice ($p < 0.001$, Fisher exact test). When background whisker noise was present, this increase in tuning scatter was even greater (59% CW-tuned in control mice vs. 44% $Cntnap2^{-/-}$ mice, $p < 0.001$).

Because of the intermixing of tuning in each column, the set of neurons tuned to any given whisker, called the tuning ensemble for that whisker, is distributed across multiple nearby columns in wild-type mice.[40–42] To test for differences in this map organization, we analyzed the spatial organization of the tuning ensemble by identifying all cells tuned to a given reference whisker, and plotting the location of these neurons relative to column boundaries defined by the L4 barrel pattern (Figures 4B and 4C). In control mice, about half of PYR neurons in a given whisker's tuning ensemble were located within that whisker's anatomical column, reflecting the distributed nature of the L2/3 whisker map (sparse conditions: 49.3%; noisy conditions: 49.9%; raw data: Figure 4B; quantification: Figure 4C). In $Cntnap2^{-/-}$ mice, this fell to 39.8% in sparse conditions and 37.4% in noisy conditions (Figure 4C). This quantification was based on 1,511, 745, 1,222 and 722 cells in control sparse, control noisy, $Cntnap2^{-/-}$ sparse, and $Cntnap2^{-/-}$ noisy conditions, respectively. This increased dispersion of the tuning ensemble in $Cntnap2^{-/-}$ was not due to different spatial sampling of imaging fields or neurons between conditions, because the subsampling of neurons to ensure an identical columnar distribution of neurons across genotypes and conditions yielded similar results (Figures S2C–S2E). Thus, the whisker map in $Cntnap2^{-/-}$ mice is even more intermixed and scattered than in control mice, with the

additional intermixing largely occurring within a whisker's home column and the near half of adjacent columns.

Consistent with fewer cells tuned for the CW in each column, the mean whisker tuning curve across all whisker-responsive cells in a column was less dominated by the CW in *Cntnap2*^{−/−} mice than in control mice, for both sparse and noisy conditions (Figure 4D). The point representation of a given whisker, defined as the tangential profile of whisker-evoked response magnitude across cortical distance in S1, was blunted in *Cntnap2*^{−/−} mice, both in sparse conditions (Figure 4E) and noisy conditions (Figures S3A and S3B). We also calculated the spatial profile of tuning preference for a given whisker, using a tuning preference index that varies between +1 (cells respond exclusively to that whisker) and −1 (cells respond exclusively to a different whisker). This tuning preference index normally falls off with cortical distance from the whisker's column center.[42] This spatial profile was blunted in *Cntnap2*^{−/−} mice in sparse conditions (Figure 4F), but not in noisy conditions (Figures S3C and S3D). Together, these findings show that the L2/3 whisker map in *Cntnap2*^{−/−} mice is blurred and weakened on the columnar level, with each column being less sharply tuned for its CW than in control mice. Background whisker noise did not alter the organization of L2/3 whisker map in control mice, but the presence of noise made the map even more dispersed in *Cntnap2*^{−/−} mice.

We also analyzed noise correlations (trial-to-trial covariability) between pairs of PYR cells.[54] Noise correlations reflect shared spontaneous activity modulation, and are often used to infer shared network connectivity. In control mice, noise correlations drop off with distance between cells.[42] *Cntnap2*^{−/−} mice showed higher noise correlations than control mice, for distances >100 μm (Figure S3E). This result may be related to the increased spontaneous activity in *Cntnap2*^{−/−} mice, and may also suggest higher local connectivity within and across columns in L2/3.

Increased tuning instability in *Cntnap2*^{−/−} mice

Sensory tuning can be unstable across days in primary sensory cortex, causing representational drift that may impact sensory computations and perception.[44,45,55] Many L2/3 PYR cells in S1 of wild-type mice exhibit unstable whisker somatotopic tuning in expert mice performing well-learned whisker tasks with stable behavior, and cells tuned to non-CWs show the highest rates of tuning instability.[42] Because *Cntnap2*^{−/−} mice have more cells tuned for non-CW whiskers (Figure 4), we hypothesized that *Cntnap2*^{−/−} mice may show more unstable whisker tuning.

To test this, we measured tuning stability in task-expert mice, by longitudinally imaging the same PYR neurons across three to four sessions spaced 4–7 days apart (Figures 5A and S4A). We compared whisker tuning of single neurons across one-, two-, or three-session intervals in control mice (1 interval: 6.0 ± 0.2 days; 2 interval: 11.9 ± 0.2 days; 3 interval: 17.9 ± 0.3 days) and *Cntnap2*^{−/−} mice (1 interval: 6.1 ± 0.1 days; 2 interval: 12.1 ± 0.2 days; 3 interval: 18.1 ± 0.4 days. These experiments were performed in four control and four *Cntnap2*^{−/−} mice in sparse stimulus conditions. Mice maintained task performance across all sessions, and the rate of spontaneous F/F events was stable across sessions, suggesting stable GCaMP8m expression (Figures S4B and S4C). In control mice, 2,155

neurons were imaged in at least two sessions and 1,632 neurons in all four sessions; in *Cntnap2*^{−/−} mice, 2,090 neurons were imaged in two or more sessions and 1,679 neurons in all four sessions. Inspection of individual fields revealed many cells that changed whisker tuning or changed whisker responsiveness across sessions. Figure 5B shows an example field from a *Cntnap2*^{−/−} mouse, with multiple cells that appear to change BW tuning (arrows) and others with stable tuning (arrowheads) across four sessions. Tuning changes are often substantial (Figure 5C), as reported previously.[42]

To study tuning instability, we first identified cells that were significantly whisker responsive across multiple sessions. In control mice, across any two sessions (1, 2, or 3 intervals), 45% of neurons were unresponsive in both sessions, 27% wavered between responsive and non-responsive, and 28% were whisker responsive in both sessions (Figure 5D). In *Cntnap2*^{−/−} mice, fewer cells were consistently whisker responsive (Figure 5D). This was also observed when analyzing 1, 2, or 3 intervals separately, or individual mice separately (Figures S4D and S4E). We analyzed the stability of whisker tuning for neurons that were responsive in any two sessions, by testing for a statistically significant change in identity of the BW (BW), defined as the emergence of a new BW that evoked responses significantly greater than the prior BW by permutation test (with $\alpha = 0.05$). This approach identifies changes in whisker responses that exceed those expected from trial-to-trial variability and finite trial number. Within a single session, 4%–5% of neurons in control mice showed a significant change in BW, as did 6%–7% of neurons in *Cntnap2*^{−/−} mice (Figure 5E, left), matching the expected false positive rate of our statistical test. Over 1, 2, or 3 intervals, 11%, 15%, and 17% of cells showed significant BW changes in control mice, respectively. Over the same intervals in *Cntnap2*^{−/−} mice, 16%, 18%, and 24% of cells showed significant BW changes. Pooling 1, 2, and 3 intervals together, *Cntnap2*^{−/−} mice showed a significantly higher fraction of cells with BW than control mice ($p = 0.001$, Fisher exact test) (Figures 5E, right, and S4F). The prevalence of BW tuning changes and whisker responsiveness changes were not correlated with variation in task engagement across sessions (Figures S5A and S5B). Thus, whisker tuning was less stable in single PYR cells in *Cntnap2*^{−/−} mice.

To test whether these tuning changes degraded the population code in S1 for whisker stimuli, we calculated the population activity vector evoked by deflection of each CW within a given imaging field. This was defined as the vector of mean Z scored F/F for each cell in the field (whether whisker responsive or not), normalized to unit length. We then computed the deviation of these population activity vectors across sessions (defined as Euclidean distance between vector endpoints).

Cntnap2^{−/−} mice showed more deviation of population vectors across sessions, indicating that population coding of whisker deflection is less stable in *Cntnap2*^{−/−} mice (Figure 5F).

In wild-type mice, whisker tuning instability is spatially organized within the L2/3 whisker map, with non-CW-tuned neurons having much more unstable tuning than CW-tuned neurons.[42] We observed this same relationship in control mice in the current dataset (Figure 5G). *Cntnap2*^{−/−} mice showed increased tuning instability for both CW- and non-CW-tuned neurons, but a particularly strong increase for non-CW-tuned neurons (Figures 5G and S5C).

Increased tuning instability in *Cntnap2*$^{-/-}$ mice was not due to broader whisker tuning or weaker BW response magnitude, which are two factors that influence tuning instability in wild-type mice (Figures S5D and S5E).[42] Thus, for *Cntnap2*$^{-/-}$ mice, excess instability occurred for neurons located both within and outside of their BW column.

Finally, we tested whether *Cntnap2*$^{-/-}$ neurons may also show more unstable response magnitude across days, distinct from unstable tuning. This hypothesis is motivated because many ASD genes are involved in activity-dependent plasticity and homeostasis,[56,57] and several ASD mouse models show impaired cellular homeostasis in sensory cortex, including *Cntnap2*$^{-/-}$.[58–60] In wild-type mice, L2/3 PYR neurons show remarkably consistent whisker-evoked response magnitude across days.[61] To test whether this is altered in *Cntnap2*$^{-/-}$ mice, we compared the BW-evoked F/F magnitude for the same cell across sessions at 1, 2, and 3 intervals. The BW response magnitude was highly correlated between sessions, both considering all cells in the imaging field or only significantly responsive cells (Figure 5H). This correlation value was not different between *Cntnap2*$^{-/-}$ and control mice for any imaging interval (Figure 5H), or when 1, 2, and 3 intervals were pooled (Figure S5F). Shuffling cell identities between sessions dropped correlation to chance, as expected (Figure S5F). Thus, *Cntnap2*$^{-/-}$ mice showed normal stability of response magnitude, even though an increased fraction of cells showed instability of whisker somatotopic tuning.

DISCUSSION

Cntnap2$^{-/-}$ mouse sensory cortex provides a strong test of the E:I ratio/hyperexcitability model of autism, because these mice exhibit clear PV hypofunction in L2/3 of sensory cortex, including reduced PV cell number, reduced feedforward inhibition, and elevated E:I ratio in S1.[13,23,30,37] While the simple prediction from the canonical E:I ratio hypothesis is hyperexcitable circuits and elevated PYR firing, synaptic excitation is also reduced onto PYR cells in *Cntnap2*$^{-/-}$ mice, which may maintain normal spiking.[13] Whether excess spiking actually occurs in *Cntnap2*$^{-/-}$ sensory cortex has been inconclusive; c-fos measurements and multi-unit recordings have suggested hyperexcitability in S1 and A1,[29,38] but single-unit recordings in S1 and V1 have shown normal and reduced sensory-evoked spike rates, respectively.[13,28] Our findings combine two-photon calcium imaging and c-fos staining to show that *Cntnap2*$^{-/-}$ mice exhibit a slight increase in spontaneous activity but not in sensory-evoked spiking in L2/3 of S1. Instead, *Cntnap2*$^{-/-}$ mice exhibit other forms of degraded neural coding, including a blurred somatotopic map, broader whisker tuning, abnormally high noise correlations, and reduced coding stability.

In our study, c-fos and GCaMP imaging gave consistent results, despite different assay conditions (anesthetized vs. awake), different activity time scales, and different cell-type specificity (both excitatory and inhibitory L2/3 cells for c-fos,[62] and excitatory L2/3 cells for Ca^{2+} imaging). Elevated spontaneous activity in *Cntnap2*$^{-/-}$ mice was evident as higher density of c-fos^{+} neurons in the unstimulated hemisphere in *Cntnap2*$^{-/-}$ vs. control mice, and increased GCaMP8m F/F signals during blank (no-stimulus) epochs. In contrast, c-fos^{+} neuron density in whisker-stimulated columns was not different between *Cntnap2*$^{-/-}$ and control, either in absolute terms or normalized to the non-stimulated hemisphere,

suggesting that raw magnitude and signal-to-noise ratio of whisker responses were not elevated. This was robustly confirmed in GCaMP8m imaging, which showed no elevation in fraction of whisker-responsive cells or whisker-evoked response magnitude (mean F/F), and even a slight depression in noisy conditions (Figures 3G, 3H, and S2B). These findings are consistent with prior *in vivo* single-unit spike recordings that showed no changes in whisker-evoked spike rate in L2/3 excitatory neurons in S1[13] and weaker visually evoked spiking in V1 of *Cntnap2*^{−/−} mice, accompanied by reduced detection sensitivity for visual stimuli.[28]

Thus, S1 and V1 of *Cntnap2*^{−/−} mice show PV hypofunction without excess PYR spiking. This is a common motif that also occurs in V1 of *Ube3a*[m−/p+] mice, V1 and whisker S1 of *Fmr1*^{−/−} mice, and V1 and S1 of *Syngap1*^{+/−} mice.[10–12,63,64] Indeed, in a broad review of ASD mouse models,[4] PV hypofunction in sensory cortex was only rarely associated with excess spiking, being observed in S1 and V1 of *Shank3b*^{−/−} mice[8,65] and in A1 and non-whisker S1 of *Fmr1*^{−/−} mice.[6,7,66] In *Cntnap2*^{−/−}, the medial prefrontal cortex also exhibits reduced synaptic inhibition[33] with normal mean firing rates during locomotion[33] and higher and more variable spontaneous activity but lower social odor-evoked responses.[67] These phenotypes resemble our findings in whisker S1. How cortex can maintain mean firing rates despite reduced inhibition may seem puzzling, but an array of homeostatic plasticity mechanisms exist in cortex that stabilize firing rate in this way.[13,68] Excess spiking eventually occurs in older *Cntnap2*^{−/−} mice in the form of spontaneous seizures.[23]

Cntnap2^{−/−} mice show atypical sensory processing for touch, audition, olfaction, and vision, including impaired auditory gap detection, impaired novel odor identification, and impaired tactile discrimination of textured objects.[17,25,29] These behaviors involve sensory discrimination and could reflect degraded discriminative coding in sensory cortex. Degraded discriminative coding might be expected because the lack of PV inhibition can acutely broaden sensory tuning of PYR cells,[69,70] and during development, PV circuits regulate the critical periods in which experience shapes precise excitatory circuits, receptive fields, and maps.[71] We observed slightly broader whisker tuning for single neurons in *Cntnap2*^{−/−} mice (Figures 3E and 3F) and substantial blurring of the whisker map due to increased intermixing of differently tuned neurons in each column (Figures 4B and 4C). This broadened the mean somatotopic tuning in each column (Figure 4D) and blunted the point representation of each whisker in S1 (Figures 4E and 4F). Because experience normally sharpens columnar organization in L2/3 of S1,[41] this degradation of the whisker map may reflect a deficit in experience-dependent refinement in *Cntnap2*^{−/−} mice.

Blurring of whisker representations was greatest under noisy sensory conditions compared to sparse conditions (Figures 3E, 3F, and 4A–4D). Noisy conditions were intended to test whether external (sensory) noise disrupts neural processing in ASD. A prominent sensory feature of ASD is difficulty in detecting speech in background noise.[72,73] This may partly reflect a higher level of endogenous neuronal noise in ASD,[1,66,74] but abnormalities in filtering out background sensory (external) noise may also occur.[75,76] Our finding that background tactile noise further degrades map topography (Figures 4B and 4C) and weakens BW response magnitude (Figure 3G) and trial-to-trial reliability (Figure 3H) suggests that inadequate filtering of external noise could contribute to coding deficits in ASD. This could

reflect a failure of sensory adaptation, inhibitory recruitment for divisive normalization, or other aspects of contextual processing.

Degraded sensory maps have been observed in $Fmr1^{-/-}$ mice,[10,13,63,77,78] $Mecp2$ overexpression mice,[79] and $En2^{-/-}$ mice,[80] and abnormally broad single-neuron sensory tuning occurs in $Fmr1^{-/-}$, $Mecp2$ deletion, and $Ube3a^{m/p+}$ mice,[9–11,64,77] but this is not universal in all ASD models.[81–84] Abnormal somatosensory maps have also been detected in people with autism.[85] These tuning and map disruptions may contribute sensory discrimination deficits in autism.[11,86,87] Our findings of broadened whisker tuning, blurred maps, and unstable somatotopic tuning in S1 of $Cntnap2^{-/-}$ mice predict behavioral impairments in somatotopic (spatial) discrimination between whiskers. Unfortunately, our all- vs. one-whisker discrimination task does not assay spatial discrimination, so whether a spatial discrimination impairment exists is unknown.

The longitudinal stability of neural coding is another factor that could impact sensory and cognitive function in ASD. In theory, excess instability in S1 could impair sensory decoding by higher cortical areas, thus blurring perception, while lower-than-normal instability could indicate overly rigid neural coding, perhaps related to behavioral rigidity or cognitive inflexibility in ASD. Tuning instability (representational drift) is common in non-topo-graphic, associative cortical areas, but also occurs in S1 and V1.[42,44,45,55] Sensory tuning drift can interfere with stable decoding of population activity in the sensory cortex,[45] although this depends on whether drift occurs in coding or non-coding population dimensions.[44] The normal function of tuning instability and representational drift is not known, but may relate to plasticity, memory consolidation, or contextual processing.[55,88]

We assessed tuning instability across 2–3 weeks in expert mice consistently performing the whisker task, and observed a significant increase in $Cntnap2^{-/-}$ mice in the fraction of L2/3 PYR cells that significantly changed their BW across sessions (Figure 5E), which increased session-to-session variability in a simple measure of whisker population coding (Figure 5F). $Cntnap2^{-/-}$ mice exhibited increased tuning instability for PYR neurons in both the columnar core and non-columnar surround of the whisker tuning ensemble.[42] Tuning instability may reflect enhanced instability at cellular and synaptic levels. Accelerated turnover of cortical dendritic spines occurs in several ASD mouse models,[89] including in $Cntnap2^{-/-}$ mice, where spines on the apical dendrite of L5b neurons show enhanced loss over a 4-day period.[90] Excess tuning instability has not been previously discovered in ASD, but would be predicted to contribute to impaired decoding of whisker identity, and thus impaired sensory discrimination.

Overall, these findings indicate that $Cntnap2^{-/-}$ mice do not exhibit hyperexcitability and excess PYR spiking in S1. Instead, these mice exhibit degraded discriminative neural coding, including broadened single-unit tuning, a blurred somatotopic map, and increased tuning instability that may impair accurate sensory discrimination or stimulus identification. If the cortex contains a blurred representation but not excess spiking or enhanced whisker representation above spontaneous noise, what is the origin of behavioral somatosensory hypersensitivity in $Cntnap2^{-/-}$ mice, including enhanced sensitivity to weak paw touch[30] and to painful stimuli?[26] We suggest that this arises from the subcortical circuits that

mediate such innate behaviors, rather than cortical circuits that are primarily responsible for complex learned behaviors and sensory perception.[4]

Limitations of the study

We did not test for a behavioral correlate of these neural coding impairments because our behavioral task was designed only to ensure that mice were alert and whisker attentive. We also do not know how near-threshold sensory representations are altered in S1, or whether cortical areas downstream of S1 show excess spiking or additional coding deficits. Our noisy sensory conditions were designed to be fairly modest (e.g., they did not impair detection of all-whisker stimuli), and a higher-noise regime, or a more difficult or near-threshold sensory task, could have revealed stronger or additional coding deficits. Because our wild-type mice were not littermates, differences in maternal care or rearing could affect our results. Finally, while PV inhibition and L2/3 PV spiking are reduced in S1 of *Cntnap2*$^{-/-}$ mice in slices and under anesthesia *in vivo*,[13] we did not verify that inhibition is reduced in the awake conditions studied here. Indeed, our finding of normal whisker-evoked response magnitude in PYR cells could indicate increased cortical inhibition[28] that may offset subcortical hyperexcitability found in some autism mouse models.[15]

STAR★METHODS

RESOURCE AVAILABILITY

Lead contact—Further information and requests for resources and reagents should be directed to and will be fulfilled by the lead contact, Dan Feldman (dfeldman@berkeley.edu).

Materials availability—This study did not generate any unique reagents.

Data and code availability

- The data reported in this paper are shared at: https://doig.org/10.17632/3n449bdt4j.1.

- The code for data analysis and examples is shared at: https://github.com/dfeldman189/Wang2024Data/tree/main/WangAnalysisCode-main.

- Any additional information or protocols required in this work paper is available from the lead contact upon request.

EXPERIMENTAL MODEL AND STUDY PARTICIPANT DETAILS

Mouse strains and conditions—Procedures were approved by the UC Berkeley Animal Care and Use Committee, and followed NIH guidelines. *Cntnap2*$^{-/-}$ (JAX 017482) and wild type *Cntnap2*$^{+/+}$ control (JAX 000664) mice were purchased from the Jackson Laboratory at 2 months of age, and were initially housed in cohorts of three or fewer mice, until craniotomy surgery at 2.5–3 months of age, after which mice were housed singly. Each cage had a running wheel (Mouse Igloo #K3327, Bio-Serv), and mice were maintained on a 12/12 light-dark cycle with humidity 30–70% and temperature 20°C–26°C. All behavior training and experiments were conducted during the dark (active) cycle. All experiments were finished before 5 months of age, to avoid the spontaneous seizures that emerge in

Cntnap2$^{-/-}$ animals over 6 months of age.[23] *Cntnap2*$^{-/-}$ mice are maintained by Jackson Laboratory on the JAX 000664 background, so these are genetically matched animals, but not littermates.

7 control and 7 *Cntnap2*$^{-/-}$ mice (5 females and 2 males in each group), were used for 2-photon imaging. Of these, 4 of each genotype were imaged in both sparse and noisy conditions, and the remainder were imaged only in sparse conditions. Longitudinal imaging was performed on a subset of these mice (4 control and 4 *Cntnap2*$^{-/-}$, [2 males and 2 females each]). It was not possible to be blind to genotype during training or imaging, because *Cntnap2*$^{-/-}$ showed behavioral differences during early head fixation training: control mice took 1–2 days for acclimation to head-fixation, while *Cntnap2*$^{-/-}$ mice typically took 3–4 days. During this delay, *Cntnap2*$^{-/-}$ mice would often freeze and not drink water from the reward port. Task learning was similar after this stage (see below). Because we could not be blind to genotype during training or imaging, we conducted each round of experiments on a yoked pair of mice, one control and one *Cntnap2*$^{-/-}$ of the same age and sex, with both receiving viral injections from the same batch of virus, to ensure matched experimental conditions between genotypes.

An additional 3 control and 3 *Cntnap2*$^{-/-}$ mice (2 male and 1 female in each group) were used for the c-fos experiments (described below).

METHOD DETAILS

Experiment design, immunolabeling, and quantification for c-fos experiments

Whisker stimulation: 3 control mice and 3 *Cntnap2*$^{-/-}$ mice were used in this experiment (2 male and 1 female in each group). Mice were lightly anesthetized with 0.5% isoflurane in O_2 combined with the sedative chlorprothixene (0.004 mg/g in normal saline, i.p.). Mice were then head-fixed and body temperature was maintained at 37°C. Whiskers A1–4, C1–4, E1–4, β and δ on the right side of the face were inserted in a piezoelectric actuator array. These constitute the stimulated whiskers. The B and D row whiskers on this same side were trimmed to prevent accidental movement by piezoelectric actuators. Whisker stimuli (trains of 5 rostrocaudal ramp-return deflections, 100-ms inter-deflection interval, 0.5-s train duration) were delivered simultaneously to all of the stimulated whiskers, every 5 s for 30 min. The whiskers on the unstimulated side of the face remained untouched.

Tissue preparation and immunolabeling for c-fos: Mice were sacrificed 60–90 min after whisker stimulation and transcardially perfused with 4% paraformaldehyde. The cortex was flattened and sectioned parallel to the cortical surface. Sections (50 μm thickness) were cut via freezing microtome and stained with anti-*c*-fos primary antibody (Cell Signaling Technology 2250T), and nuclei were stained with 4′,6-diamidino-2-phenylindole (DAPI). Barrels were labeled with fluorescent streptavidin (Streptavidin, Alexa Fluor 647 conjugate, S21374).[48] Confocal z-stacks (z-step size, 1 μm) of each section were obtained using a 20× objective (Plan Apo VC 20× DIC N2) on a Nikon spinning disc confocal microscope (Eclipse Ti microscope with Andor DU-897 camera) with NIS-Elements AR software.

Quantification of c-fos-positive cells: Cell counting and analysis were performed with ImageJ (NIH, Bethesda). c-fos positive cells were counted manually in each 50-μm section through L2/3 (defined as the 5 50-μm sections spanning the 250 μm immediately above L4). Images were aligned to column boundaries from streptavidin staining of barrels in L4, using blood vessels as landmarks. Counting was performed manually by navigating through the z stack. Only cells within column borders were counted (i.e., ignoring cells located above septa). Cell counting was done blind to genotype. Cell density (c-fos positive cells per mm^3) was calculated by summing counted cells across sections, and normalizing to column area and total 250 μm depth. Cell density was compared between stimulated (A-C-E) and unstimulated (B-D) columns in the stimulated hemisphere, and these same columns in the non-stimulated hemisphere. For each whisker row A-E, all individual cortical columns within that row were combined to a single point representing that row in Figures 1D and 1E.

Cranial window surgery and viral injection—At 2.5–3 months of age, mice were anesthetized with isoflurane (1–1.5% in O$_2$) and dexamethasone (2 mg/kg), enrofloxican (5 mg/kg), and meloxicam (10 mg/kg) were administered. A stainless-steel head holder with 6 mm aperture was affixed to the skull using cyanoacrylate glue and dental cement. The D1–3 whisker columns in S1 were localized using transcranial intrinsic signal optical imaging.[91,92] A 3 mm diameter craniotomy was made centered on the D2 column. We used two viral strategies to express GCaMP8m in L2/3 PYR neurons. In some mice (2 control and 2 *Cntnap2*$^{-/-}$), we co-injected AAV9-*syn*-jGCaMP8m-WPRE (Addgene # 162375-AAV9, 6×10^{12} GC/ml) and AAV1-mDlx-NLS-mRuby2 (Addgene #99130-AAV1, 1×10^{13} GC/ml) to drive pan-neuronal expression of GCaMP8m and interneuron-specific expression of mRuby2.[93] We imaged GCaMP8m in the green channel and mRuby2 in the red channel, and only analyzed mRuby2-negative neurons. In the remaining mice, we co-injected with AAV1-*syn*-FLEX-jGCaMP8m-WPRE (Addgene # 162378-AAV1, 6×10^{12} GC/ml) and AAV9.CamKII 0.4.Cre.SV40 (Addgene # 105558-AAV9, 1×10^{13} GC/ml), which limits GCAMP8m expression to excitatory neurons. Both viral strategies yielded similar results for genotype effects on whisker-evoked response magnitude, tuning width, and map organization, and thus the data were combined.

AAV injections were made at 250 μm and 350 μm subpial depth, at 3–4 locations in S1 surrounding the D2 column. At each injection site, 46 nL of AAV solution was injected at 23 nl/s. After AAV injection, a chronic cranial window (3 mm diameter glass coverslip, #1 thickness, CS-3R, Warner Instrument) was attached with dental cement. After surgery, buprenorphine (0.1 mg/kg) was administered for post-operative analgesia.

Behavioral apparatus and behavioral monitoring—Mice performed the behavioral task daily, 5 days per week. At the start of each behavior session, mice were transiently anesthetized with isoflurane and head-fixed under the 2-photon microscope. 9 whiskers (rows C-E, arcs 1–3) were inserted into a 3 × 3 array of calibrated piezoelectric actuators, centered on the D2 whisker. Whiskers were not trimmed, and were threaded into tubes on the piezos, held by soft glue. Deflections were applied 5 mm from the face. A drink port with capacitive lick sensor recorded licks. Paw guards prevented paw contact with whiskers,

piezos, or drink port. After whisker insertion, anesthesia was stopped, and mice recovered from anesthesia and began the behavioral task (typically 15 min after stopping isoflurane).

Training was performed in total visual darkness (using 850 nm IR illumination for behavioral monitoring). Uniform white noise (77.4 ± 0.5 dB) was continuously applied to mask sounds from piezo actuators and drink port opening. The task was controlled by an Arduino Mega 2560, which monitored licking, dispensed reward, and governed trial timing, with online user control via custom routines in Igor Pro (WaveMetrics). Mice self-initiated each trial by suppressing licking (inter-lick interval >4000 ms). A given behavioral session used either sparse stimulus trials, or noisy stimulus trials (see below).

For quantification of behavioral performance, d-prime for detection of S+ stimuli were defined as:

$$d' = z(\text{hit}) - z(\text{false alarm})$$

where z = inverse of the normal cumulative distribution function with mean = 0 and standard deviation = 1. Reaction time was defined as the time between the onset of whisker cue and the first lick in hit trials.

Sparse session trial structure: Each trial consisted of a 1 s baseline period, 1.5 s pre-stimulus period, 0.5 s whisker cue stimulus period, and 1.5 s response window. One randomly chosen stimulus was applied per trial: either one of the 9 single whisker cues, the all-whisker deflection, or a blank (no stimulus). Whisker cue stimuli consisted of ramp-return rostrocaudal deflections (300 μm, 5 ms rise/fall time, 10 ms duration), applied in a train of 5 deflections (100 ms inter-pulse interval, 500 ms train duration). Trains were used because they evoked more reliable GCaMP signals in L2/3 neurons than single-deflection stimuli. The all-whisker stimulus consisted of simultaneous whisker cue stimuli delivered across all 9 whiskers.

The response window began at the end of the whisker cue deflection. On S+ trials (all-whisker stimuli), water reward (2–4 μL) was automatically dispensed 300 ms into the response window. Licking was not required to dispense reward. Water was not dispensed on S− trials. Licking above a threshold rate (2 licks with <400 ms inter-lick interval) during the response window was defined as a lick response, and scored as a hit on S+ trials and a false alarm (FA) on S− trials. Response latency was defined as the time of the first of these 2 licks. FAs and misses were not rewarded or punished. Each trial was followed by a 2 ± 1 s inter-trial interval (ITI) before the mouse could initiate the next trial. Thus, whisker stimuli were separated by > 6.5 ± 1 s in the sparse condition.

Noisy session trial structure: For noisy stimulus sessions, trial structure was the same as for sparse stimulus sessions, except that random, small-amplitude, single-whisker deflections (90 μm, which was 30% of whisker cue stimulus amplitude) were applied every 200 ± 100 ms on every trial. These noise stimuli were applied on randomly interleaved whiskers, and started during the prestimulus period and lasted till the end of trial, including the whisker cue stimulus period. No whisker noise was applied during inter-trial intervals or

during the baseline period at the start of each trial. All whiskers were randomly interleaved for noise stimuli, independent of which whisker was chosen for the main whisker cue stimulus on that trial.

Noisy sessions were not presented during initial training. Once mice were trained, noisy sessions were presented on a subset of days for Ca^{2+} imaging, intermixed with sparse stimulus sessions.

Training stages—1–2 weeks after cranial window implantation, mice began water regulation to provide motivation for training. Daily water intake was reduced to an individually determined volume (0.7–1.0 mL) to achieve 85% of ad lib body weight. Mice received water rewards for correct responses during training, and the balance of the water budget was provided after each training session. Mice had free access to food, and weight and health were monitored daily.

Training and imaging were conducted in parallel for each pair of control and *Cntnap2*−/− mice. Training proceeded in stages. In Stage 1 training, mice were acclimated to head-fixation and presence of the water port. *Cntnap2*−/− mice took consistently longer to habituate to head fixation, which prevented the experimenter from being blind to genotype. In Stage 2, mice learned to lick for water rewards (2–4 μL) cued by a blue LED mounted on the lick port. In Stage 3, S+/S− training began, using only all-whisker deflection (S+) and blank stimuli (S−). The LED still flashed at the time of water delivery. Over days, mice learned to lick to the S+ stimulus, evidenced by an advance in lick timing from after LED onset to before LED onset, as well as by a reduction in FA licks on S− trials. This training stage continued until FA rate fell below 50%, and >50% of licks on S+ trials occurred prior to the LED cue. In Stage 4, the final full behavioral task was implemented by introducing the other 9 S− stimuli and removing the LED cue. Training was only performed using sparse stimulus conditions.

Imaging sessions began when mice reached stable Stage 4 performance with >900 trials per session, including ~10–20% S+ trials. Whiskers were not trimmed, and remained intact throughout the experiment.

Two photon imaging—2-photon imaging took place 4–6 weeks after viral injection. Imaging was performed with a Moveable Objective Microscope (Sutter) and Chameleon Ultra II Ti:Sapphire mode-locked laser (Coherent). GCaMP8m and mRuby2 were excited at 920 nm. Scanning utilized one resonant scanner (RESSCAN-MOM, Sutter) and one galvo scanner (Cambridge Technology). Emission was collected through a 16× immersion objective (0.8 NA, N16XLWD-PF, Nikon), bandpass-filtered with dichroic mirrors (green channel: HQ 575/50, red channel: HQ 610/75, Chroma), and GaAsP photomultiplier tubes (H10770PA-40, Hamamatsu). Laser power at the sample was 30–75 mW. Serial single plane images (512 × 512 pixels, 150–275 μm below dura) were acquired at 7.5 Hz (30 Hz acquisition, 4-frame average) using ScanImage5.6[94] (Vidrio). Fields of view of either 305 μm × 305 μm or 406 μm × 406 μm were used.

Each daily session comprised 900–1000 trials. In each mouse, 2–5 different imaging fields were sampled in each type of behavioral session (sparse and noisy). We did not directly compare sparse and noisy conditions in the same field of view. In total, 17 imaging fields were obtained from *Cntnap2$^{+/+}$* mice under sparse conditions, 13 fields from *Cntnap2$^{+/+}$* under noisy conditions, 16 fields from *Cntnap2$^{-/-}$* under sparse conditions, and 11 fields from *Cntnap2$^{-/-}$* under noisy conditions. Longitudinal imaging was performed on 2 *Cntnap2$^{+/+}$* and 2 *Cntnap2$^{-/-}$* mice. For longitudinal imaging, 3–4 fields were imaged in each mouse, only under sparse conditions, with each field re-imaged 3–4 times at 4–7-day intervals.

Histological localization of 2-photon imaging fields and cells—Cells imaged in 2-photon experiments were localized relative to L4 barrel boundaries using post-hoc histology. A 2-photon z stack was collected spanning from the L2/3 imaging plane to the pial surface, at the end of each imaging session. After imaging experiments were complete, the brain was removed and fixed in 4% paraformaldehyde, and the cortex was flattened and serially sectioned (50 μm thickness) parallel to the cortical surface, with individual sections spanning from the surface blood vessels down through L4. These sections were stained for cytochrome oxidase activity or with fluorophore tagged streptavidin (Streptavidin, Alexa Fluor 647 conjugate, S21374).[48] Both of these methods reveal L4 barrels. Sections were digitized and barrel boundaries traced from the L4 sections and aligned to the surface vessels. Imaging fields were then aligned to column boundaries using blood vessels as landmarks.

QUANTIFICATION AND STATISTICAL ANALYSIS

Calcium imaging analysis—Analysis used the CaImAn[95] algorithm and custom MATLAB routines unless stated otherwise.

Imaging processing and ROI selection: Movies were corrected for slow X-Y motion using NoRMCorre.[96] Substantial z axis movement was not observed and not corrected. Neuronal regions-of-interests (ROIs) were defined using CaImAn with default settings. The CaImAn algorithm recognized 80% of visible cells, and remaining cells were manually annotated using CaImAn's manually_refine_components function based on the average image. F/F traces were extracted by CaImAn, with F_0 defined as the 25th percentile of the fluorescence distribution for that ROI. Only ROIs near stimulated whisker columns were analyzed (defined as 1.25 barrel radii from the centroid of a stimulated whisker column). We manually inspected and removed neurons with their nuclei filled with GCaMP, which indicated overexpression. Around 5% of neurons were removed from each imaging field. The total number of imaged neurons were: *Cntnap2$^{+/+}$* sparse: 2751; *Cntnap2$^{+/+}$* noisy: 1583; *Cntnap2$^{-/-}$* sparse: 2136; *Cntnap2$^{-/-}$* noisy: 1815. For longitudinal imaging, we also examined the spontaneous event rate through the imaging sessions and found the population spontaneous activity remained constant (Figure S4B), suggesting stable GCaMP expression.

Whisker-evoked responses and receptive fields: To avoid lick contamination, F/F responses were only analyzed on non-lick trials. Stimulus-evoked F/F was defined as mean F/F (0–1000 ms after stimulus onset) minus mean baseline F/F. To identify significant

whisker responses, we used a permutation test for difference in mean ΔF/F for each whisker relative to blank trials. In each iteration of the permutation test, single-trial ΔF/F data were randomly shuffled between whisker S− and blank trials, and the difference in mean response between these shuffled trial sets was calculated. This was repeated 10,000 times to generate a null distribution. A measured whisker response was considered significant if it exceeded the 95th percentile of this null distribution. p-values were corrected for multiple comparisons across all S− stimuli with false discovery rate 0.05 (Benjamini-Hochberg procedure).[97] A cell was considered whisker-responsive if $\geq$ 1 whisker induced a significant positive ΔF/F response. A single trial was defined as responsive if stimulus-evoked ΔF/F exceeded the mean plus one standard deviation of blank trials.

Negative ΔF/F responses were replaced with zero.

Tuning of individual neurons: The best whisker (BW) was defined as the whisker that evoked the largest mean ΔF/F response and was significantly greater than blanks. For a cell to be classified as non-CW-tuned, the non-CW response had to be statistically greater than the CW response. BW tuning sharpness (Figure 3F) was defined as $(R_{BW} - R_W)/(R_{BW} + R_W)$, where R_{BW} = mean ΔF/F to BW, and R_W = averaged mean ΔF/F for all other whiskers (whiskers that evoked a negative response were considered as zero). Columnar whisker (CW) preference (Figures 4F and 4–Figures S2C and S2D) was calculated similarly as $(R_{CW} - R_W)/(R_{CW} + R_W)$, where R_{CW} = ΔF/F to the CW. Rank-ordered tuning curves were calculated by ranking each stimulus from strongest to weakest within each cell (normalizing to the blank) and then averaging ranked tuning curves across cells. This quantifies tuning sharpness around each cell's BW, independent of somatotopic organization. For rank-ordered tuning curves, only cells whose BW was the center whisker or a center-edge whisker in the piezo array were included. This ensures that the BW plus 5 or 8 immediate adjacent whisker responses were sampled.

Normalized anatomical reference frame for spatial analysis across imaging fields: To project cells into a common columnar coordinate system, ROI coordinates were transformed into a polar reference frame. We first drew a vector from the centroid of a reference column to the ROI. The normalized distance from ROI to column center was calculated as (measured distance)/(distance from column center to column edge along this vector). This gives units of barrel column radii. To determine the angular position for each ROI, vectors were drawn connecting the centroid of each surrounding column to the centroid of the reference column. These vectors defined equally spaced 45° angles in reference space, and ROI angle was determined relative to these vectors.

Analysis of tuning stability by longitudinal imaging: ROIs were identified independently for each imaging session by CaImAn. ROIs that corresponded to the same neuron across sessions were registered manually based on the average image for each session. 80.6% of imaged neurons could be traced in at least 2 out of 4 sessions. Neurons that could not be traced tended to be close to the imaging field edge and were obscured by image registration, or exhibited very low activity and thus did not appear in average image.

To assess tuning stability across sessions, we tested for a statistically significant change in BW, by testing whether a new whisker evoked a significantly stronger mean ΔF/F than the prior BW, assessed by permutation test.

When neurons were present across all 4 sessions, each neuron could contribute 3 different Δ1 measurements (1st→2nd, 2nd→3rd, and 3rd→4th), 2 different Δ2 measurements (1st→3rd, 2nd→4th) and one Δ3 measurement (1st→4th). To avoid overcounting the same cell in Δ1 and Δ2 measurements, we randomly subsampled a single Δ1 or Δ2 value for each cell, repeated this 1000 times, and reported mean and 95% confidence interval for these measurements (error bars or shadings in Figures 5F, S4D, and S4E).

<u>Population activity vector:</u> To evaluate the stability of single whisker representation in L2/3 across sessions, we calculated the population activity vector elicited by deflection of a single whisker in each session. For a given whisker whose column was present in the imaging field, the mean responses of each cell in the imaging field (N cells) to that whisker were concatenated as an Nx1 vector, and normalized by the L2 norm of the vector. The population activity vector was also calculated in the next imaging session, using the same cells. The Euclidean distance between the two vectors (Δ population vector) was used to quantify the change of single whisker representation in that cell population across sessions. If an imaging field contained more than one whisker column, the Δ population vector was determined by averaging the Δ population vectors for each whisker that was present.

<u>Spatial subsampling of ROIs:</u> We validated the whisker map differences between genotypes by performing additional analysis to correct for modest differences in spatial distribution of imaged neurons. To do so, we subsampled the data to generate spatially identical sampling in both genotypes. In each iteration of subsampling, cells were randomly chosen from *Cntnap2*$^{+/+}$ or *Cntnap2*$^{-/-}$ mice so that the numbers of cells within each whisker column were the same. Data analysis was done for these subsampled cells. We performed 1000 iterations of this subsampling. The resulting mean and 95% confidence intervals are reported in Figures S2A and S2B.

Statistics

Statistical methods are described in Figure Legends and above. Sample size was not pre-determined. All tests were two-tailed except for permutation tests. Single neurons were unit N, except as follows: Mouse behavior was quantified by mouse and by behavioral session (Figures 2C–2E, S4A, and S4B). The fraction of responsive neurons per imaging field, spontaneous activity in longitudinal imaging, and population vectors were analyzed by imaging field (Figures 3D, 5F, and S4C). c-fos quantification was quantified by row and side (Figures 1D and 1E).

In violin plots, circle is median, horizontal line is mean, thick vertical line is interquartile range, and thin vertical line is 1.5× interquartile range (Figure 3F).

Abbreviations: KS, Kolmogorov-Smirnoff test. $\chi2$, chi-squared test. Rank-sum, Wilcoxon rank-sum test. Data are presented as mean ± standard error of mean (SEM), except where noted.

Supplementary Material

Refer to Web version on PubMed Central for supplementary material.

ACKNOWLEDGMENTS

REFERENCES

1. Rubenstein JLR, and Merzenich MM (2003). Model of autism: increased ratio of excitation/inhibition in key neural systems. Genes Brain Behav. 2, 255–267. [PubMed: 14606691]

2. Sohal VS, and Rubenstein JLR (2019). Excitation-inhibition balance as a framework for investigating mechanisms in neuropsychiatric disorders. Mol. Psychiatry 24, 1248–1257. 10.1038/s41380-019-0426-0. [PubMed: 31089192]

3. Levy SE, Mandell DS, and Schultz RT (2009). Autism. Lancet 374, 1627–1638. [PubMed: 19819542]

4. Monday HR, Wang HC, and Feldman DE (2023). Circuit-level theories for sensory dysfunction in autism: convergence across mouse models. Front. Neurol 14, 1254297. 10.3389/fneur.2023.1254297. [PubMed: 37745660]

5. Gonçalves JT, Anstey JE, Golshani P, and Portera-Cailliau C (2013). Circuit level defects in the developing neocortex of Fragile X mice. Nat. Neurosci 16, 903–909. 10.1038/nn.3415. [PubMed: 23727819]

6. Rotschafer SE, and Razak KA (2014). Auditory processing in fragile x syndrome. Front. Cell. Neurosci 8, 19. 10.3389/fncel.2014.00019. [PubMed: 24550778]

7. Zhang Y, Bonnan A, Bony G, Ferezou I, Pietropaolo S, Ginger M, Sans N, Rossier J, Oostra B, LeMasson G, and Frick A (2014). Dendritic channelopathies contribute to neocortical and sensory hyperexcitability in Fmr1(–/y) mice. Nat. Neurosci 17, 1701–1709. 10.1038/nn.3864. [PubMed: 25383903]

8. Chen Q, Deister CA, Gao X, Guo B, Lynn-Jones T, Chen N, Wells MF, Liu R, Goard MJ, Dimidschstein J, et al. (2020). Dysfunction of cortical GABAergic neurons leads to sensory hyper-reactivity in a Shank3 mouse model of ASD. Nat. Neurosci 23, 520–532. 10.1038/s41593-020-0598-6. [PubMed: 32123378]

9. Banerjee A, Rikhye RV, Breton-Provencher V, Tang X, Li C, Li K, Runyan CA, Fu Z, Jaenisch R, and Sur M (2016). Jointly reduced inhibition and excitation underlies circuit-wide changes in cortical processing in Rett syndrome. Proc. Natl. Acad. Sci. USA 113, E7287–E7296. 10.1073/pnas.1615330113. [PubMed: 27803317]

10. Juczewski K, von Richthofen H, Bagni C, Celikel T, Fisone G, and Krieger P (2016). Somatosensory map expansion and altered processing of tactile inputs in a mouse model of fragile X syndrome. Neurobiol. Dis 96, 201–215. 10.1016/j.nbd.2016.09.007. [PubMed: 27616423]

11. Goel A, Cantu DA, Guilfoyle J, Chaudhari GR, Newadkar A, To-disco B, de Alba D, Kourdougli N, Schmitt LM, Pedapati E, et al. (2018). Impaired perceptual learning in a mouse model of Fragile X syndrome is mediated by parvalbumin neuron dysfunction and is reversible. Nat. Neurosci 21, 1404–1411. 10.1038/s41593-018-0231-0. [PubMed: 30250263]

12. Michaelson SD, Ozkan ED, Aceti M, Maity S, Llamosas N, Weldon M, Mizrachi E, Vaissiere T, Gaffield MA, Christie JM, et al. (2018). SYNGAP1 heterozygosity disrupts sensory processing by reducing touch-related activity within somatosensory cortex circuits. Nat. Neurosci 21, 1–13. 10.1038/s41593-018-0268-0.

13. Antoine MW, Langberg T, Schnepel P, and Feldman DE (2019). Increased Excitation-Inhibition Ratio Stabilizes Synapse and Circuit Excitability in Four Autism Mouse Models. Neuron 101, 648–661.e4. 10.1016/j.neuron.2018.12.026. [PubMed: 30679017]

14. Robertson CE, and Baron-Cohen S (2017). Sensory perception in autism. Nat. Rev. Neurosci 18, 671–684. 10.1038/nrn.2017.112. [PubMed: 28951611]

15. Orefice LL, Mosko JR, Morency DT, Wells MF, Tasnim A, Mozeika SM, Ye M, Chirila AM, Emanuel AJ, Rankin G, et al. (2019). Targeting Peripheral Somatosensory Neurons to Improve Tactile-Related Phenotypes in ASD Models. Cell 178, 867–886.e24. 10.1016/j.cell.2019.07.024. [PubMed: 31398341]

16. Schaffler MD, Middleton LJ, and Abdus-Saboor I (2019). Mechanisms of Tactile Sensory Phenotypes in Autism: Current Understanding and Future Directions for Research. Curr. Psychiatry Rep 21, 134. 10.1007/s11920-019-1122-0. [PubMed: 31807945]

17. Gordon A, Salomon D, Barak N, Pen Y, Tsoory M, Kimchi T, and Peles E (2016). Expression of Cntnap2 (Caspr2) in multiple levels of sensory systems. Mol. Cell. Neurosci 70, 42–53. 10.1016/j.mcn.2015.11.012. [PubMed: 26647347]

18. Bonetto G, Hivert B, Goutebroze L, Karagogeos D, Crépel V, and Faivre-Sarrailh C (2019). Selective Axonal Expression of the Kv1 Channel Complex in Pre-myelinated GABAergic Hippocampal Neurons. Front. Cell. Neurosci 13, 222. 10.3389/fncel.2019.00222. [PubMed: 31164806]

19. Alarcón M, Abrahams BS, Stone JL, Duvall JA, Perederiy JV, Bomar JM, Sebat J, Wigler M, Martin CL, Ledbetter DH, et al. (2008). Linkage, association, and gene-expression analyses identify CNTNAP2 as an autism-susceptibility gene. Am. J. Hum. Genet 82, 150–159. 10.1016/j.ajhg.2007.09.005. [PubMed: 18179893]

20. Arking DE, Cutler DJ, Brune CW, Teslovich TM, West K, Ikeda M, Rea A, Guy M, Lin S, Cook EH, and Chakravarti A (2008). A common genetic variant in the neurexin superfamily member CNTNAP2 increases familial risk of autism. Am. J. Hum. Genet 82, 160–164. 10.1016/j.ajhg.2007.09.015. [PubMed: 18179894]

21. Bakkaloglu B, O'Roak BJ, Louvi A, Gupta AR, Abelson JF, Morgan TM, Chawarska K, Klin A, Ercan-Sencicek AG, Stillman AA, et al. (2008). Molecular cytogenetic analysis and resequencing of contactin associated protein-like 2 in autism spectrum disorders. Am. J. Hum. Genet 82, 165–173. 10.1016/j.ajhg.2007.09.017. [PubMed: 18179895]

22. Poliak S, Salomon D, Elhanany H, Sabanay H, Kiernan B, Pevny L, Stewart CL, Xu X, Chiu S-Y, Shrager P, et al. (2003). Juxtaparanodal clustering of Shaker-like K+ channels in myelinated axons depends on Caspr2 and TAG-1. J. Cell Biol 162, 1149–1160. 10.1083/jcb.200305018. [PubMed: 12963709]

23. Peñagarikano O, Abrahams BS, Herman EI, Winden KD, Gdalyahu A, Dong H, Sonnenblick LI, Gruver R, Almajano J, Bragin A, et al. (2011). Absence of CNTNAP2 leads to epilepsy, neuronal migration abnormalities, and core autism-related deficits. Cell 147, 235–246. 10.1016/j.cell.2011.08.040. [PubMed: 21962519]

24. Brunner D, Kabitzke P, He D, Cox K, Thiede L, Hanania T, Sabath E, Alexandrov V, Saxe M, Peles E, et al. (2015). Comprehensive Analysis of the 16p11.2 Deletion and Null Cntnap2 Mouse Models of Autism Spectrum Disorder. PLoS One 10, e0134572. [PubMed: 26273832]

25. Truong DT, Rendall AR, Castelluccio BC, Eigsti I-M, and Fitch RH (2015). Auditory processing and morphological anomalies in medial geniculate nucleus of Cntnap2 mutant mice. Behav. Neurosci 129, 731–743. 10.1037/bne0000096. [PubMed: 26501174]

26. Dawes JM, Weir GA, Middleton SJ, Patel R, Chisholm KI, Pettingill P, Peck LJ, Sheridan J, Shakir A, Jacobson L, et al. (2018). Immune or Genetic-Mediated Disruption of CASPR2 Causes Pain Hypersensitivity Due to Enhanced Primary Afferent Excitability. Neuron 97, 806–822.e10. 10.1016/j.neuron.2018.01.033. [PubMed: 29429934]

27. Scott R, Sánchez-Aguilera A, van Elst K, Lim L, Dehorter N, Bae SE, Bartolini G, Peles E, Kas MJH, Bruining H, and Marín O (2019). Loss of Cntnap2 Causes Axonal Excitability Deficits, Developmental Delay in Cortical Myelination, and Abnormal Stereotyped Motor Behavior. Cereb. Cortex 29, 586–597. 10.1093/cercor/bhx341. [PubMed: 29300891]

28. Del Rosario J, Speed A, Arrowood H, Motz C, Pardue M, and Haider B (2021). Diminished Cortical Excitation and Elevated Inhibition During Perceptual Impairments in a Mouse Model of Autism. Cereb. Cortex 31, 3462–3474. 10.1093/cercor/bhab025. [PubMed: 33677512]

29. Balasco L, Pagani M, Pangrazzi L, Chelini G, Viscido F, Chama AGC, Galbusera A, Provenzano G, Gozzi A, and Bozzi Y (2022). Somatosensory cortex hyperconnectivity and impaired whisker-dependent responses in Cntnap2(−/−) mice. Neurobiol. Dis 169, 105742. 10.1016/j.nbd.2022.105742. [PubMed: 35483565]

30. Deemyad T, Puig S, Papale AE, Qi H, LaRocca GM, Aravind D, LaNoce E, and Urban NN (2022). Lateralized Decrease of Parvalbumin+ Cells in the Somatosensory Cortex of ASD Models Is Correlated with Unilateral Tactile Hypersensitivity. Cereb. Cortex 32, 554–568. 10.1093/cercor/bhab233. [PubMed: 34347040]

31. Jurgensen S, and Castillo PE (2015). Selective Dysregulation of Hippocampal Inhibition in the Mouse Lacking Autism Candidate Gene CNTNAP2. J. Neurosci 35, 14681–14687. 10.1523/JNEUROSCI.1666-15.2015. [PubMed: 26511255]

32. Bridi MS, Park SM, and Huang S (2017). Developmental Disruption of GABAAR-Meditated Inhibition in Cntnap2 KO Mice. eNeuro 4, ENEURO.0162–17.2017.

33. Lazaro MT, Taxidis J, Shuman T, Bachmutsky I, Ikrar T, Santos R, Marcello GM, Mylavarapu A, Chandra S, Foreman A, et al. (2019). Reduced Prefrontal Synaptic Connectivity and Disturbed Oscillatory Population Dynamics in the CNTNAP2 Model of Autism. Cell Rep 27, 2567–2578.e6. [PubMed: 31141683]

34. Sacai H, Sakoori K, Konno K, Nagahama K, Suzuki H, Watanabe T, Watanabe M, Uesaka N, and Kano M (2020). Autism spectrum disorder-like behavior caused by reduced excitatory synaptic transmission in pyramidal neurons of mouse prefrontal cortex. Nat. Commun 11, 5140. 10.1038/s41467-020-18861-3. [PubMed: 33046712]

35. Paterno R, Marafiga JR, Ramsay H, Li T, Salvati KA, and Baraban SC (2021). Hippocampal gamma and sharp-wave ripple oscillations are altered in a Cntnap2 mouse model of autism spectrum disorder. Cell Rep. 37, 109970. 10.1016/j.celrep.2021.109970. [PubMed: 34758298]

36. Lauber E, Filice F, and Schwaller B (2018). Dysregulation of Parvalbumin Expression in the Cntnap2−/− Mouse Model of Autism Spectrum Disorder. Front. Mol. Neurosci 11, 262. 10.3389/fnmol.2018.00262. [PubMed: 30116174]

37. Vogt D, Cho KKA, Shelton SM, Paul A, Huang ZJ, Sohal VS, and Rubenstein JLR (2018). Mouse Cntnap2 and Human CNTNAP2 ASD Alleles Cell Autonomously Regulate PV+ Cortical Interneurons. Cereb. Cortex 28, 3868–3879. 10.1093/cercor/bhx248. [PubMed: 29028946]

38. Scott KE, Mann RS, Schormans AL, Schmid S, and Allman BL (2022). Hyperexcitable and Immature-Like Neuronal Activity in the Auditory Cortex of Adult Rats Lacking the Language-Linked CNTNAP2 Gene. Cereb. Cortex 32, 4797–4817. 10.1093/cercor/bhab517. [PubMed: 35106542]

39. Woolsey TA, and Van der Loos H (1970). The structural organization of layer IV in the somatosensory region (SI) of mouse cerebral cortex. The description of a cortical field composed of discrete cytoarchitectonic units. Brain Res. 17, 205–242. [PubMed: 4904874]

40. Clancy KB, Schnepel P, Rao AT, and Feldman DE (2015). Structure of a single whisker representation in layer 2 of mouse somatosensory cortex. J. Neurosci 35, 3946–3958. 10.1523/JNEUROSCI.3887-14.2015. [PubMed: 25740523]

41. LeMessurier AM, Laboy-Juárez KJ, McClain K, Chen S, Nguyen T, and Feldman DE (2019). Enrichment drives emergence of functional columns and improves sensory coding in the whisker map in L2/3 of mouse S1. Elife 8, e46321. [PubMed: 31418693]

42. Wang HC, LeMessurier AM, and Feldman DE (2022). Tuning instability of non-columnar neurons in the salt-and-pepper whisker map in somatosensory cortex. Nat. Commun 13, 6611. 10.1038/s41467-022-34261-1. [PubMed: 36329010]

43. Ziv Y, Burns LD, Cocker ED, Hamel EO, Ghosh KK, Kitch LJ, El Gamal A, and Schnitzer MJ (2013). Long-term dynamics of CA1 hippocampal place codes. Nat. Neurosci 16, 264–266. [PubMed: 23396101]

44. Deitch D, Rubin A, and Ziv Y (2021). Representational drift in the mouse visual cortex. Curr. Biol 31, 4327–4339.e6. 10.1016/j.cub.2021.07.062. [PubMed: 34433077]

45. Schoonover CE, Ohashi SN, Axel R, and Fink AJP (2021). Representational drift in primary olfactory cortex. Nature 594, 541–546. 10.1038/s41586-021-03628-7. [PubMed: 34108681]

46. Dragunow M, and Faull R (1989). The use of c-fos as a metabolic marker in neuronal pathway tracing. J. Neurosci. Methods 29, 261–265. 10.1016/0165-0270(89)90150-7. [PubMed: 2507830]

47. Filipkowski RK, Rydz M, Berdel B, Morys J, and Kaczmarek L (2000). Tactile experience induces c-fos expression in rat barrel cortex. Learn. Mem 7, 116–122. 10.1101/lm.7.2.116. [PubMed: 10753978]

48. Sumser A, Mease RA, Sakmann B, and Groh A (2017). Organization and somatotopy of corticothalamic projections from L5B in mouse barrel cortex. Proc. Natl. Acad. Sci. USA 114, 8853–8858. 10.1073/pnas.1704302114. [PubMed: 28774955]

49. Pluta SR, Lyall EH, Telian GI, Ryapolova-Webb E, and Adesnik H (2017). Surround Integration Organizes a Spatial Map during Active Sensation. Neuron 94, 1220–1233.e5. 10.1016/j.neuron.2017.04.026. [PubMed: 28504117]

50. Zhang Y, Rózsa M, Liang Y, Bushey D, Wei Z, Zheng J, Reep D, Broussard GJ, Tsang A, Tsegaye G, et al. (2023). Fast and sensitive GCaMP calcium indicators for imaging neural populations. Nature 615, 884–891. 10.1038/s41586-023-05828-9. [PubMed: 36922596]

51. Golshani P, Gonçalves JT, Khoshkhoo S, Mostany R, Smirnakis S, and Portera-Cailliau C (2009). Internally mediated developmental desynchronization of neocortical network activity. J. Neurosci 29, 10890–10899. 10.1523/JNEUROSCI.2012-09.2009. [PubMed: 19726647]

52. O'Connor DH, Peron SP, Huber D, and Svoboda K (2010). Neural activity in barrel cortex underlying vibrissa-based object localization in mice. Neuron 67, 1048–1061. 10.1016/j.neuron.2010.08.026. [PubMed: 20869600]

53. Crochet S, Poulet JFA, Kremer Y, and Petersen CCH (2011). Synaptic mechanisms underlying sparse coding of active touch. Neuron 69, 1160–1175. 10.1016/j.neuron.2011.02.022. [PubMed: 21435560]

54. Kohn A, Coen-Cagli R, Kanitscheider I, and Pouget A (2016). Correlations and Neuronal Population Information. Annu. Rev. Neurosci 39, 237–256. 10.1146/annurev-neuro-070815-013851. [PubMed: 27145916]

55. Driscoll LN, Duncker L, and Harvey CD (2022). Representational drift: Emerging theories for continual learning and experimental future directions. Curr. Opin. Neurobiol 76, 102609. 10.1016/j.conb.2022.102609. [PubMed: 35939861]

56. Nelson SB, and Valakh V (2015). Excitatory/Inhibitory balance and circuit homeostasis in Autism Spectrum Disorders. Neuron 87, 684–698. 10.1016/j.neuron.2015.07.033. [PubMed: 26291155]

57. Mullins C, Fishell G, and Tsien RW (2016). Unifying Views of Autism Spectrum Disorders: A Consideration of Autoregulatory Feedback Loops. Neuron 89, 1131–1156. 10.1016/j.neuron.2016.02.017. [PubMed: 26985722]

58. Blackman MP, Djukic B, Nelson SB, and Turrigiano GG (2012). A critical and cell-autonomous role for MeCP2 in synaptic scaling up. J. Neurosci 32, 13529–13536. 10.1523/JNEUROSCI.3077-12.2012. [PubMed: 23015442]

59. Fernandes D, Santos SD, Coutinho E, Whitt JL, Beltrão N, Rondão T, Leite MI, Buckley C, Lee H-K, and Carvalho AL (2019). Disrupted AMPA Receptor Function upon Genetic- or Antibody-Mediated Loss of Autism-Associated CASPR2. Cereb. Cortex 29, 4919–4931. 10.1093/cercor/bhz032. [PubMed: 30843029]

60. Tatavarty V, Torrado Pacheco A, Groves Kuhnle C, Lin H, Koundinya P, Miska NJ, Hengen KB, Wagner FF, Van Hooser SD, and Turrigiano GG (2020). Autism-Associated Shank3 Is Essential for Homeostatic Compensation in Rodent V1. Neuron 106, 769–777.e4. 10.1016/j.neuron.2020.02.033. [PubMed: 32199104]

61. Margolis DJ, Lütcke H, Schulz K, Haiss F, Weber B, Kügler S, Hasan MT, and Helmchen F (2012). Reorganization of cortical population activity imaged throughout long-term sensory deprivation. Nat. Neurosci 15, 1539–1546. 10.1038/nn.3240. [PubMed: 23086335]

62. Staiger JF, Masanneck C, Bisler S, Schleicher A, Zuschratter W, and Zilles K (2002). Excitatory and inhibitory neurons express c-Fos in barrel-related columns after exploration of a novel environment. Neuroscience 109, 687–699. 10.1016/s0306-4522(01)00501-2. [PubMed: 11927151]

63. Arnett MT, Herman DH, and McGee AW (2014). Deficits in Tactile Learning in a Mouse Model of Fragile X Syndrome. PLoS One 9, e109116. 10.1371/journal.pone.0109116. [PubMed: 25296296]

64. Wallace ML, van Woerden GM, Elgersma Y, Smith SL, and Philpot BD (2017). Ube3a loss increases excitability and blunts orientation tuning in the visual cortex of Angelman syndrome model mice. J. Neurophysiol 118, 634–646. 10.1152/jn.00618.2016. [PubMed: 28468997]

65. Pagano J, Landi S, Stefanoni A, Nardi G, Albanesi M, Bauer HF, Pracucci E, Schön M, Ratto GM, Boeckers TM, et al. (2023). Shank3 deletion in PV neurons is associated with abnormal behaviors

and neuronal functions that are rescued by increasing GABAergic signaling. Mol. Autism 14, 28. 10.1186/s13229-023-00557-2. [PubMed: 37528484]

66. Bhaskaran AA, Gauvrit T, Vyas Y, Bony G, Ginger M, and Frick A (2023). Endogenous noise of neocortical neurons correlates with atypical sensory response variability in the Fmr1(–/y) mouse model of autism. Nat. Commun 14, 7905. 10.1038/s41467-023-43777-z. [PubMed: 38036566]

67. Levy DR, Tamir T, Kaufman M, Parabucki A, Weissbrod A, Schneidman E, and Yizhar O (2019). Dynamics of social representation in the mouse prefrontal cortex. Nat. Neurosci 22, 2013–2022. 10.1038/s41593-019-0531-z. [PubMed: 31768051]

68. Gainey MA, and Feldman DE (2017). Multiple shared mechanisms for homeostatic plasticity in rodent somatosensory and visual cortex. Philos. Trans. R. Soc. Lond. B Biol. Sci 372, 20160157. [PubMed: 28093551]

69. Atallah BV, Bruns W, Carandini M, and Scanziani M (2012). Parvalbumin-expressing interneurons linearly transform cortical responses to visual stimuli. Neuron 73, 159–170. 10.1016/j.neuron.2011.12.013. [PubMed: 22243754]

70. Aizenberg M, Mwilambwe-Tshilobo L, Briguglio JJ, Natan RG, and Geffen MN (2015). Bidirectional Regulation of Innate and Learned Behaviors That Rely on Frequency Discrimination by Cortical Inhibitory Neurons. PLoS Biol. 13, e1002308. 10.1371/journal.pbio.1002308. [PubMed: 26629746]

71. Hensch TK (2005). Critical period plasticity in local cortical circuits. Nat. Rev. Neurosci 6, 877–888. [PubMed: 16261181]

72. Alcántara JI, Weisblatt EJL, Moore BCJ, and Bolton PF (2004). Speech-in-noise perception in high-functioning individuals with autism or Asperger's syndrome. J. Child Psychol. Psychiatry 45, 1107–1114. 10.1111/j.1469-7610.2004.t01-1-00303.x. [PubMed: 15257667]

73. Schelinski S, and von Kriegstein K (2020). Brief Report: Speech-in-Noise Recognition and the Relation to Vocal Pitch Perception in Adults with Autism Spectrum Disorder and Typical Development. J. Autism Dev. Disord 50, 356–363. 10.1007/s10803-019-04244-1. [PubMed: 31583624]

74. Simmons DR, Robertson AE, McKay LS, Toal E, McAleer P, and Pollick FE (2009). Vision in autism spectrum disorders. Vision Res. 49, 2705–2739. 10.1016/j.visres.2009.08.005. [PubMed: 19682485]

75. Park WJ, Schauder KB, Zhang R, Bennetto L, and Tadin D (2017). High internal noise and poor external noise filtering characterize perception in autism spectrum disorder. Sci. Rep 7, 17584. 10.1038/s41598-017-17676-5. [PubMed: 29242499]

76. Mihaylova MS, Bocheva NB, Totev TT, and Staykova SN (2021). Visual Noise Effect on Contour Integration and Gaze Allocation in Autism Spectrum Disorder. Front. Neurosci 15, 623663. 10.3389/fnins.2021.623663. [PubMed: 33633537]

77. Rotschafer S, and Razak K (2013). Altered auditory processing in a mouse model of fragile X syndrome. Brain Res. 1506, 12–24. 10.1016/j.brainres.2013.02.038. [PubMed: 23458504]

78. He Q, Arroyo ED, Smukowski SN, Xu J, Piochon C, Savas JN, Portera-Cailliau C, and Contractor A (2019). Critical period inhibition of NKCC1 rectifies synapse plasticity in the somatosensory cortex and restores adult tactile response maps in fragile X mice. Mol. Psychiatry 24, 1732–1747. 10.1038/s41380-018-0048-y. [PubMed: 29703945]

79. Zhou C, Yan S, Qian S, Wang Z, Shi Z, Xiong Y, and Zhou Y (2019). Atypical Response Properties of the Auditory Cortex of Awake MECP2-Overexpressing Mice. Front. Neurosci 13, 439. 10.3389/fnins.2019.00439. [PubMed: 31133783]

80. Allegra M, Genovesi S, Maggia M, Cenni MC, Zunino G, Sgadò P, Caleo M, and Bozzi Y (2014). Altered GABAergic markers, increased binocularity and reduced plasticity in the visual cortex of Engrailed-2 knockout mice. Front. Cell. Neurosci 8, 163. 10.3389/fncel.2014.00163. [PubMed: 24987331]

81. Garcia-Junco-Clemente P, Chow DK, Tring E, Lazaro MT, Trachtenberg JT, and Golshani P (2013). Overexpression of calcium-activated potassium channels underlies cortical dysfunction in a model of PTEN-associated autism. Proc. Natl. Acad. Sci. USA 110, 18297–18302. 10.1073/pnas.1309207110. [PubMed: 24145404]

82. Krishnan K, Wang B-S, Lu J, Wang L, Maffei A, Cang J, and Huang ZJ (2015). MeCP2 regulates the timing of critical period plasticity that shapes functional connectivity in primary visual cortex. Proc. Natl. Acad. Sci. USA 112, E4782–E4791. 10.1073/pnas.1506499112. [PubMed: 26261347]

83. Ortiz-Cruz CA, Marquez EJ, Linares-García CI, Perera-Murcia GR, and Ramiro-Cortés Y (2022). Haploinsufficiency of Shank3 increases the orientation selectivity of V1 neurons. Sci. Rep 12, 22230. 10.1038/s41598-022-26402-9. [PubMed: 36564435]

84. Wadle SL, Schmitt TTX, Engel J, Kurt S, and Hirtz JJ (2023). Altered population activity and local tuning heterogeneity in auditory cortex of Cacna2d3-deficient mice. Biol. Chem 404, 607–617. 10.1515/hsz-2022-0269. [PubMed: 36342370]

85. Coskun MA, Varghese L, Reddoch S, Castillo EM, Pearson DA, Loveland KA, Papanicolaou AC, and Sheth BR (2009). How somatic cortical maps differ in autistic and typical brains. Neuroreport 20, 175–179. 10.1097/WNR.0b013e32831f47d1. [PubMed: 19057419]

86. Puts NAJ, Wodka EL, Tommerdahl M, Mostofsky SH, and Edden RAE (2014). Impaired tactile processing in children with autism spectrum disorder. J. Neurophysiol 111, 1803–1811. 10.1152/jn.00890.2013. [PubMed: 24523518]

87. He JL, Wodka E, Tommerdahl M, Edden RAE, Mikkelsen M, Mostofsky SH, and Puts NAJ (2021). Disorder-specific alterations of tactile sensitivity in neurodevelopmental disorders. Commun. Biol 4, 97. 10.1038/s42003-020-01592-y. [PubMed: 33483581]

88. Micou C, and O'Leary T (2023). Representational drift as a window into neural and behavioural plasticity. Curr. Opin. Neurobiol 81, 102746. 10.1016/j.conb.2023.102746. [PubMed: 37392671]

89. Nakai N, Takumi T, Nakai J, and Sato M (2018). Common Defects of Spine Dynamics and Circuit Function in Neurodevelopmental Disorders: A Systematic Review of Findings From in Vivo Optical Imaging of Mouse Models. Front. Neurosci 12, 412. 10.3389/fnins.2018.00412. [PubMed: 29970983]

90. Gdalyahu A, Lazaro M, Penagarikano O, Golshani P, Trachtenberg JT, and Geschwind DH (2015). The Autism Related Protein Contactin-Associated Protein-Like 2 (CNTNAP2) Stabilizes New Spines: An In Vivo Mouse Study. PLoS One 10, e0125633. 10.1371/journal.pone.0125633. [PubMed: 25951243]

91. Grinvald A, Lieke E, Frostig RD, Gilbert CD, and Wiesel TN (1986). Functional architecture of cortex revealed by optical imaging of intrinsic signals. Nature 324, 361–364. 10.1038/324361a0. [PubMed: 3785405]

92. Drew PJ, and Feldman DE (2009). Intrinsic signal imaging of deprivation-induced contraction of whisker representations in rat somatosensory cortex. Cereb. Cortex 19, 331–348. 10.1093/cercor/bhn085. [PubMed: 18515797]

93. Chan KY, Jang MJ, Yoo BB, Greenbaum A, Ravi N, Wu W-L, Sánchez-Guardado L, Lois C, Mazmanian SK, Deverman BE, and Gradinaru V (2017). Engineered AAVs for efficient noninvasive gene delivery to the central and peripheral nervous systems. Nat. Neurosci 20, 1172–1179. 10.1038/nn.4593. [PubMed: 28671695]

94. Pologruto TA, Sabatini BL, and Svoboda K (2003). ScanImage: flexible software for operating laser scanning microscopes. Biomed. Eng. Online 2, 13. 10.1186/1475-925X-2-13. [PubMed: 12801419]

95. Giovannucci A, Friedrich J, Gunn P, Kalfon J, Brown BL, Koay SA, Taxidis J, Najafi F, Gauthier JL, Zhou P, et al. (2019). CaImAn an open source tool for scalable calcium imaging data analysis. Elife 8, e38173. 10.7554/eLife.38173. [PubMed: 30652683]

96. Pnevmatikakis EA, and Giovannucci A (2017). NoRMCorre: An online algorithm for piecewise rigid motion correction of calcium imaging data. J. Neurosci. Methods 291, 83–94. 10.1016/j.jneumeth.2017.07.031. [PubMed: 28782629]

97. Benjamini Y, Drai D, Elmer G, Kafkafi N, and Golani I (2001). Controlling the false discovery rate in behavior genetics research. Behav. Brain Res 125, 279–284. 10.1016/s0166-4328(01)00297-2. [PubMed: 11682119]

Highlights

- Characterizes sensory coding in S1 cortex in the *Cntnap2*$^{-/-}$ mouse model of autism

- Broad tuning and blurred, unstable maps, but no excess sensory-evoked spiking

- Reduced inhibition is associated with degraded, unstable sensory coding in *Cntnap2*$^{-/-}$ mice
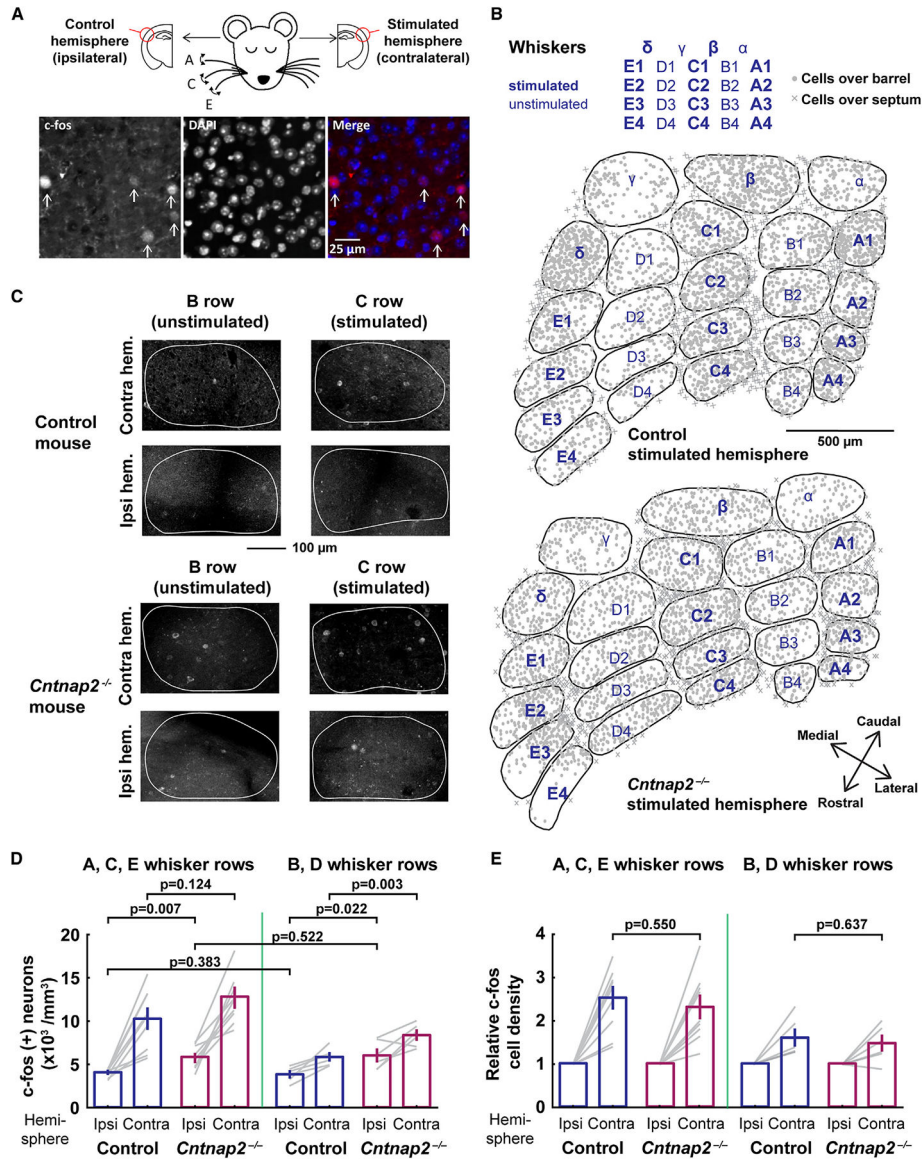
Figure 1. Spontaneous and whisker-evoked c-fos expression in L2/3 of S1 in control and *Cntnap2*$^{-/-}$ mice

(A) Top: design of c-fos immunolabeling experiment. Bottom: examples of cells co-labeled with c-fos and nuclear stain (DAPI).

(B) Locations of all c-fos$^+$ L2/3 neurons relative to L4 barrel boundaries in the contralateral (stimulated) hemisphere from one control and one Cntnap2$^{-/-}$ mouse. Data were compiled across 250 μm in L2/3.

(C) Example sections showing c-fos staining in L2/3 of single columns in two example mice. White outline is column boundary from L4.

(D) Density of c-fos$^+$ cells in L2/3 of S1, comparing stimulated and unstimulated hemisphere, across all mice. Each gray line is one column (A, B, C, D, or E) in one mouse. *p* values are for genotype factor in unbalanced two-way ANOVA.

(E) Same data as (D), normalized to the unstimulated hemisphere of each mouse. *p* values are for genotype factor in unbalanced two-way ANOVA.
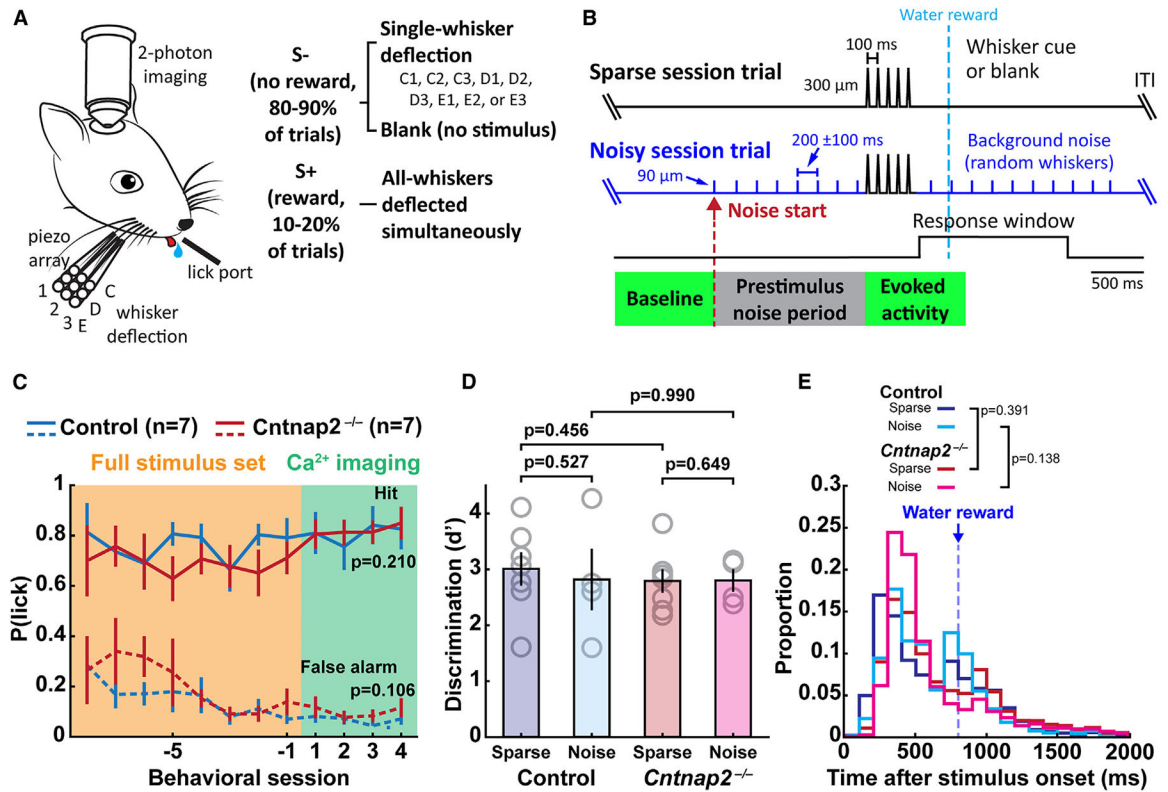
Figure 2. Behavioral task for receptive field mapping in awake mice

(A) Experiment design and setup, showing stimuli and reward assignment for the task.

(B) Trial structure for sparse and noisy sessions.

(C) Behavioral performance during training, once all S+ and S– stimuli are present (orange, showing the last eight sessions prior to imaging), and once mice have achieved expert performance and imaging begins (green, showing the first four imaging sessions). *p* values are for genotype factor in unbalanced two-way ANOVA.

(D) Behavioral discrimination performance (d-prime) during imaging sessions, by genotype and noise condition. Statistics: rank-sum.

(E) Reaction time (first lick time) for hit trials, by genotype and noise condition. Statistics: rank-sum. All error bars are SEM.

See also Figure S1.
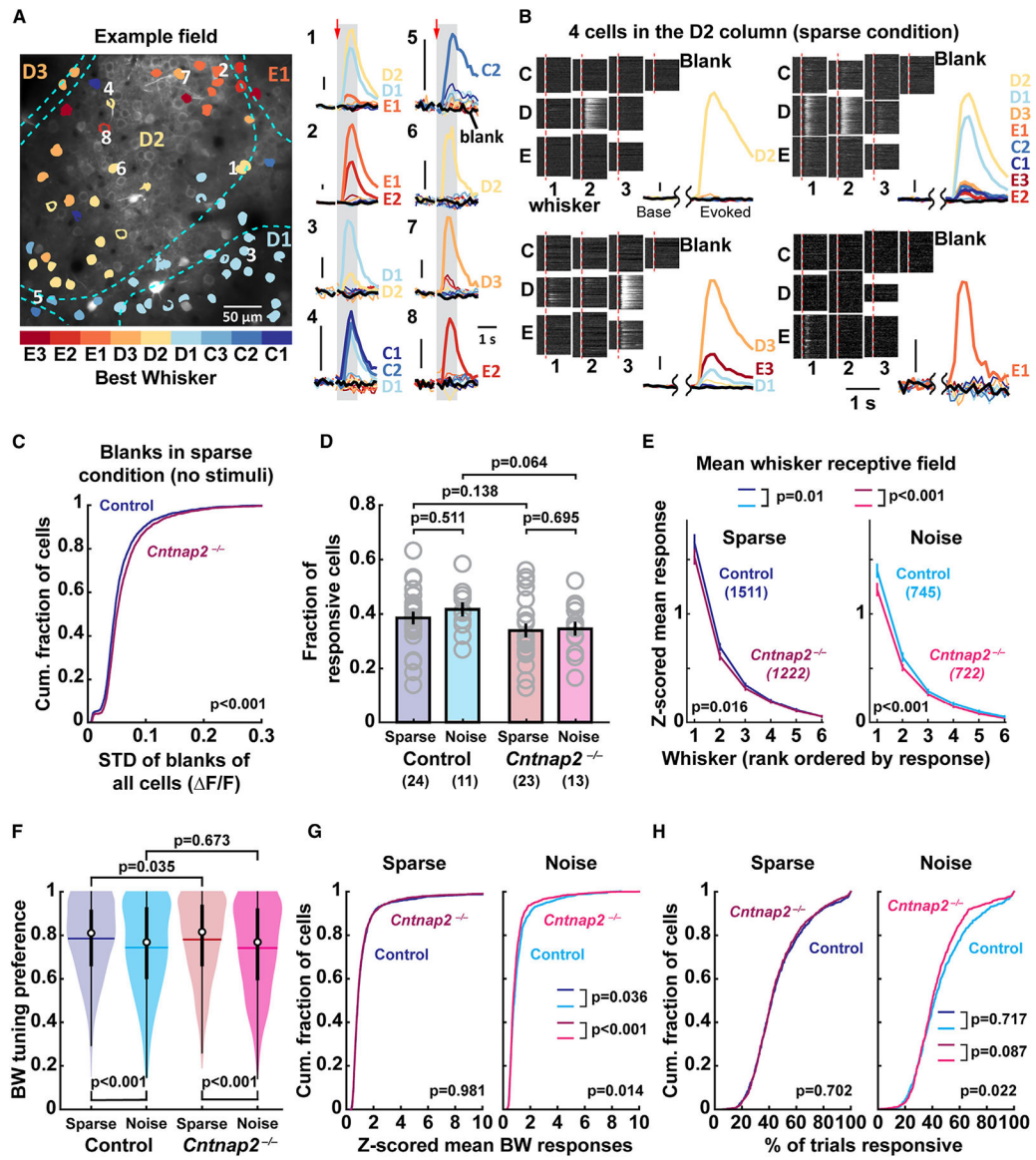
Figure 3. Whisker responsiveness and tuning of L2/3 PYR neurons in control and *Cntnap2*^{−/−} mice

(A) Example imaging field showing GCaMP8m-expressing PYR cells color-coded for their BW. Dashed lines, column boundaries from L4. Right: mean whisker-evoked ΔF/F traces for example cells 1–8. Thick traces and whisker labels show significant whisker responses; thin traces are non-significant responses; black traces are blanks. Arrows show whisker deflection onset. Gray, response analysis window. Scale bar: 0.1 ΔF/F.

(B) Whisker tuning and trial-to-trial reliability for four example cells imaged in the D2 column. Left, ΔF/F traces for each single-whisker trial and blank trial. Dash, stimulus onset. ΔF/F traces are normalized to maximum for each cell. Right, mean ΔF/F traces across trials. Base, baseline period. Evoked, evoked period. The prestimulus noise period is omitted for clarity. Scale bar: 0.1 ΔF/F.

(C) Standard deviation (STD) of responses in blank trials in sparse conditions (calculated across trials), as a measure of spontaneous activity. Statistics: Kolmogorov-Smirnov.

(D) Fraction of whisker-responsive neurons in each imaging field, by genotype and noise condition. Each circle is one imaging field. Statistics: rank-sum.

(E) Mean rank-ordered whisker-tuning curves across all whisker-responsive neurons. Only cells whose BW and at least five adjacent whiskers were sampled were included. Responses are Z scored to activity in blank trials. Error bars: SEM. p values are for genotype or noise level factor in unbalanced two-way ANOVA.

(F) Distribution of mean BW tuning preference of responsive neurons. Circles are medians, horizontal lines are means, thick vertical lines are interquartile ranges, and thin vertical line is 1.5× interquartile ranges. Statistics: rank-sum.

(G) The cumulative distribution of Z scored BW responses of responsive neurons. Statistics: Kolmogorov-Smirnov.

(H) Cumulative fraction of individual trials with significant whisker response. Statistics: Kolmogorov-Smirnov.

See also Figure S2.
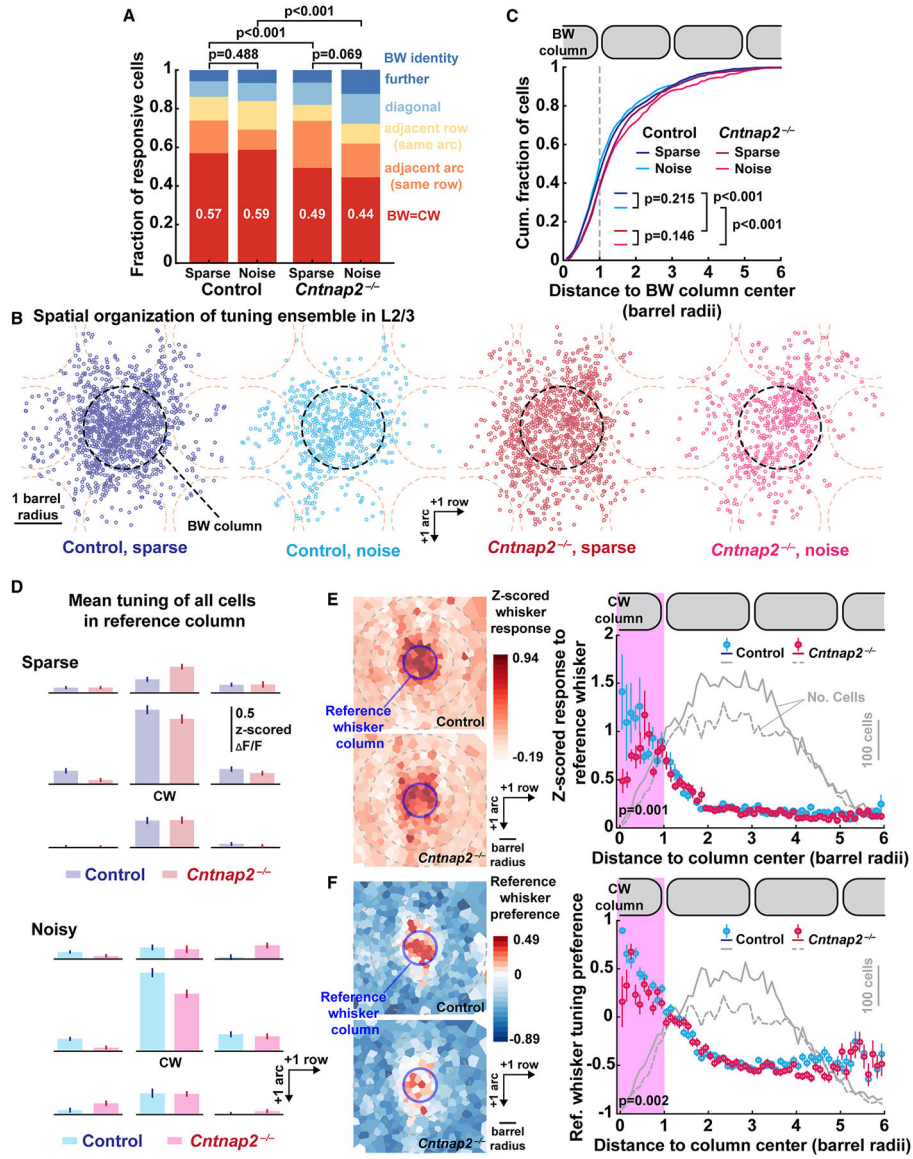
Figure 4. Blurred whisker map in L2/3 of *Cntnap2*−/− mice

(A) BW identity for all responsive cells in a whisker column, by genotype and noise condition. Cell numbers (left to right): 1,204, 634, 957, and 607. Statistics: Fisher's exact test for BW = CW or not.

(B) Spatial distribution of the tuning ensemble in control and *Cntnap2*−/− mice. Each panel shows the location of each PYR neuron relative to its BW column. Cell numbers (left to right): 1,511, 745, 1,222, and 722. Dashed circles show the average location of nearby columns.

(C) Distance of each responsive cell from its BW column center. Statistics: Kolmogorov-Smirnov.

(D) Mean whisker-tuning curve for all responsive cells in a column. Whiskers are shown somatotopically, with the CW in the center. Responses were *Z* scored to spontaneous activity in each cell.

(E) Left: two-dimensional (2D) spatial distribution of evoked responses to a given reference whisker, normalized to spontaneous activity in each cell. Cell location is plotted relative to the reference whisker column. Cells were spatially binned using k-means clustering so that each polygonal bin contains 20 cells. Colors show mean CW-evoked response for all cells in the bin. Right: average response magnitude to the reference whisker for all whisker-responsive neurons, binned by cell distance to the reference whisker column center. This shows the point representation of a whisker among all whisker-responsive cells in L2/3. Error bars: SEM. Statistics: rank-sum for data within the whisker column.

(F) Left: 2D spatial distribution of tuning preference to a reference whisker, plotted as in (E). Color indicates mean CW preference index in each bin. Right: average preference for a reference whisker among all whisker-responsive neurons, binned by cell distance from the reference whisker column center. This quantifies the tuning gradient across all whisker-responsive neurons. Plotting and statistics as in (E).

See also Figure S2.
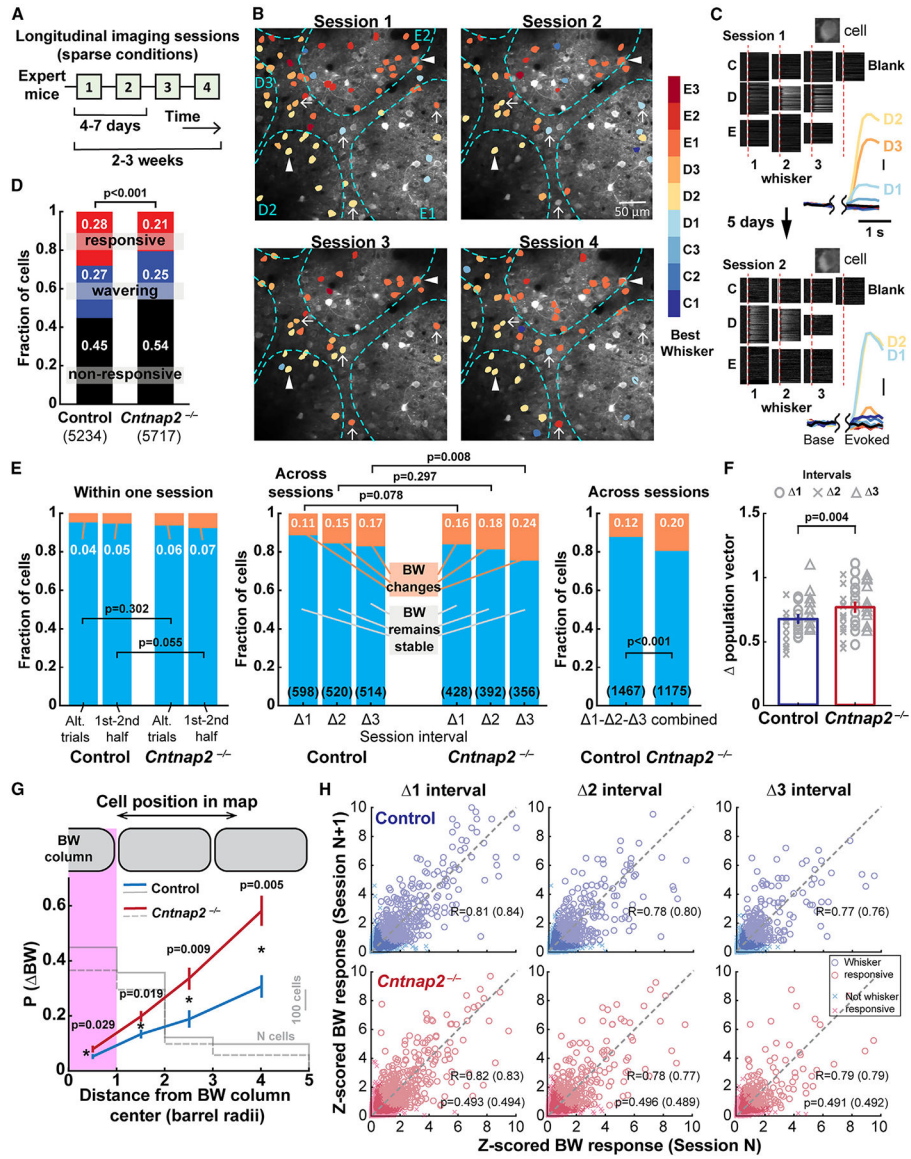
Figure 5. *Cntnap2*^{−/−} mice have less stable whisker tuning

(A) Time line of longitudinal imaging sessions from one imaging field.

(B) Example of four-session longitudinal imaging from one field, showing barrel boundaries and GCaMP8m-expressing PYR cells color-coded for their BW identity in each session. Arrows: cells changed their BW at least once across four sessions. Arrowhead: cells kept their BW in all sessions.

(C) Example cell showing receptive field change between sessions. Conventions as in Figure 3B.

(D) Changes in responsiveness for cells tracked longitudinally. Black, unresponsive in both sessions. Red, responsive in both sessions. Blue, responsive in one session only. All intervals were pooled. Numbers are fractions of cells. *n*: pairs. Statistics: χ^2.

(E) The proportion of stably responsive cells whose BW significantly changed within or across sessions. Left: BW changes within the same session. Center: changes over Δ1, Δ2,

or 3 session intervals. Right: changes pooled over all intervals. *n*: pairs. Statistics: Fisher's exact test for BW changes or not.

(F) Mean change in whisker-evoked population activity vectors across sessions. See text for explanation. Error bars: SEM. *p* value is for genotype factor in unbalanced two-way ANOVA.

(G) Mean fraction of neurons exhibiting a BW change, as a function of cell distance to its BW column center in session one. Cells in the magenta area were initially CW-tuned. Data pooled across different intervals. Statistics: rank-sum test between the two genotypes within each bin. Lines with error bars are mean and bootstrapped 95% confidence intervals after subsampling to ensure each cell is represented only once. Asterisks indicate significant difference after multiple comparison test.

(H) Correlation of Z scored BW responses in one session with the next session, separated by 1, 2, or 3 session intervals. R: Pearson's correlation coefficient for all cells and responsive cells (in parentheses). Statistics: permutation test between genotypes.

See also Figures S4 and S5.

KEY RESOURCES TABLE

REAGENT or RESOURCE	SOURCE	IDENTIFIER
Antibodies		
Rabbit anti-*c*-Fos antibody	Cell Signaling	#2250
Streptavidin, Alexa Fluor™ 647 conjugate	Invitrogen	S21374; RRID:AB_2336066
Bacterial and virus strains		
AAV9-*syn*-jGCaMP8m-WPRE	Zhang et al.[50]	162375-AAV9; RRID:Addgene_162375
AAV1-mDlx-NLS-mRuby2	Chan et al.[93]	99130-AAV1; RRID:Addgene_99130
AAV1-*syn*-FLEX-jGCaMP8m-WPRE	Zhang et al.[50]	162378-AAV1; RRID:Addgene_162378
AAV9.CamKII 0.4.Cre.SV40	a gift from James M. Wilson	105558-AAV9; RRID:Addgene_105558
Deposited data		
Raw data	This paper	Mendeley Data, https://doi.org/10.17632/3n449bdt4j.1
Experimental models: Organisms/strains		
Mouse: C57BL/6J	The Jackson Laboratory	JAX 000664
Mouse: B6.129(Cg)-Cntnap2[tm1Pele]/J	The Jackson Laboratory	JAX 017482
Software and algorithms		
MATLAB R2022a	MathWorks	RRID:SCR_001622
Igor Pro 6	WaveMetrics	RRID:SCR_000325
ScanImage 5.6	Vidrio	RRID:SCR_014307